Master Thesis

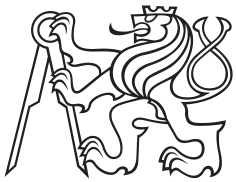

Czech
Technical
University
in Prague

F4

Faculty of Nuclear Sciences and Physical Engineering
Department of Physics

Optimisation of processing raw data from Thomson scattering diagnostic on the COMPASS tokamak

Bc. Miroslav Šos

Supervisor: Ing. Petr Böhm, Ph.D.
Field of study: Physics and Thermonuclear Fusion Technology
May 2018

ČESKÉ VYSOKÉ UČENÍ TECHNICKÉ V PRAZE
FAKULTA JADERNÁ A FYZIKÁLNĚ INŽENÝRSKÁ
PRAHA 1 - STARÉ MĚSTO, BŘEHOVÁ 7 - PSČ 115 19

Katedra: fyziky *Akademický rok:* 2017/18

ZADÁNÍ DIPLOMOVÉ PRÁCE

Student: Bc. Miroslav Šos

Studijní program: Aplikace přírodních věd

Obor: Fyzika a technika termojaderné fúze

Název práce: (česky) Optimalizace zpracování dat z diagnostiky Thomsonova rozptylu na tokamaku COMPASS

Název práce: (anglicky) Optimisation of processing raw data from Thomson scattering diagnostic on the COMPASS tokamak

Pokyny pro vypracování:

Soubor rutin pro zpracování hrubých dat z diagnostiky Thomsonova rozptylu (TS, Thomson scattering) na tokamaku COMPASS byl převzat roku 2011, kdy byl systém uváděn do provozu. Od té doby bylo na systému provedeno mnoho změn a rozšíření. Cílem práce je vytvořit zcela nový soubor rutin zpracování dat v "open source" programovacím jazyce Python, přičemž je kladen důraz na vyšší modularitu a variabilitu celého systému. Především v částech, kde se provádí fitování naměřených dat, je požadována větší robustnost. Bude také provedena kontrola a revize kalibrací systému TS.

Jednotlivé úkoly:

1) Vyvinout a implementovat výpočetní kód pro TS
   - fitování rychlého signálu v časové oblasti
   - propojení s výsledky kalibrací
   - výpočet elektronové hustoty a teploty
   - správné určení chyb měření a uložení výsledků do databáze
2) Kontrola a revize souboru kalibrací - případně provedení nových metod kalibrace

Doporučená literatura:

[1] S. L. Prunty: A primer on the theory of Thomson scattering for high-temperature fusion plasmas. Phys. Scr. 89 (2014)

[2] K. Miyamoto: Plasma Physics for Controlled Fusion, Springer Series on Atomic, Optical, and Plasma Phys. Springer-Verlag Berlin Heidelberg, 2016

[3] J. Sheffield, et al.: Plasma Scattering of Electromagnetic Radiation. Academic Press, 2011

[4] Wes McKinney: Python for Data Analysis, O´Reilly Media, 2012

[5] R. Scannell: Investigation of H-mode edge profile behaviour on MAST using Thomson scattering. PhD thesis, (2007)

Jméno a pracoviště vedoucího diplomové práce:

Ing. Petr Böhm, Ph.D.
Ústav fyziky plazmatu Akademie věd České republiky, v.v.i.

Datum zadání diplomové práce: 31.10.2017

Termín odevzdání diplomové práce: 07.05.2018

Doba platnosti zadání je dva roky od data zadání.

…….. ……..
vedoucí katedry *děkan*

V Praze dne 31.10.2017

Acknowledgements

I would like to thank my supervisor Ing. Petr Böhm, Ph.D. for his everlasting patience and support, for his enlightening insights and precious suggestions. This thesis would have never come into existence without all his help. I would also like to thank RNDr. Petra Bílková, Ph.D. for her advices, assistance and making me part of the team, which made me feel more at home. I would like to express my gratitude to my friend Ondřej Grover for his undying patience, while responding to the endless number of questions and cries for help throughout our studies.

Furthermore, I would like to thank my family and close ones for their support, encouragement and making me laugh even during times that were not very cheerful.

Last but not least, I would like to thank Matěj Tomeš for his valuable insights and comments while reading this thesis; you know I owe you a beer now, or more likely two.

Declaration

I hereby declare, that I have written this thesis by myself and I have used only the materials stated in the references section.

I have no reason to object to use this work according to the section 60 of Act No. 121/2000 Coll.,On Copyright, on Rights Related to Copyright, and on Change of Some Acts (Copyright Act)

Prague, May 7, 2018

Abstract

The Thomson scattering (TS) diagnostic is one of the key diagnostics used on both recent and planned for the future tokamaks. Its complexity and high demanding character are balanced by its invaluable ability to measure electron temperature and density profiles without perturbing the plasma. In the first part the theoretical background of TS is covered and the realization is demonstrated on the TS diagnostic on the COMPASS tokamak.

Second part is devoted to the data processing system and innovative contributions to the diagnostic's calibration. The implementation of individual segments of the deeply analysed data processing algorithm, including complex calibration process, fitting of the raw data from the fast data acquisition and the very calculation of electron temperature and density, is described. The system performance is validated comparing both partial and final results with the current processing unit. Within the last section, concerning optimization of the spatial calibration method called „split-fibre", the correlation between the movement of laser beam image on the collection fibre bundle and vibrations of the collection optics was found.

Keywords: thermonuclear fusion, tokamak COMPASS, Thomson scattering diagnostics, data processing, Python

Supervisor: Ing. Petr Böhm, Ph.D.
Tokamak department
Institute of Plasma Physics of the Czech Academy of Sciences

Abstrakt

Diagnostika Thomsonova rozptylu (TS) je jednou z klíčových diagnostik na současných i plánovaných tokamacích do budoucna. Vysoké nároky a složitost diagnostiky vynahrazuje neocenitelná schopnost měřit profil elektronové teploty a hustoty, aniž by docházelo k narušení plazmatu. V první části práce jsou shrnuty teoretické poznatky z teorie TS. Následně je představena realizace diagnostiky na tokamaku COMPASS.

Druhá část je věnována procesu zpracování dat a inovativním příspěvkům ke kalibracím diagnostiky. Implementace dílčích segmentů detailně analyzovaného algoritmu zpracování dat, zahrnující komplexní proces souboru kalibrací, fitování hrubých dat z rychlých datových sběrů a vlastní výpočet elektronové teploty a hustoty, je zde popsána. Ověření získaných dílčích i finálních výsledků nově implementovaného systému je provedeno porovnáním s výsledky současného zpracování dat. V rámci závěrečné části zabývající se optimalizací prostorové kalibrace diagnostiky metodou „split-fibre" byla zjištěna korelace mezi pohybem obrazu laserového pulsu po svazku sběrných optických vláken a vibracemi sběrné optické soustavy.

Klíčová slova: Termojaderná fúze, tokamak COMPASS, diagnostika Thomsonova rozptylu, zpracování dat, Python

Překlad názvu: Optimalizace zpracování dat z diagnostiky Thomsonova rozptylu na tokamaku COMPASS

Contents

Chapter 1

Introduction

Reliable diagnostic system is the fundamental aspect of each experimental research device, including tokamak. It can be also stated that the physics research on such a device can be only as good as the information provided by its diagnostics. Tokamak reactors represent the leading concept in pursuit of the thermonuclear fusion energy source; possibly a stable and profitable source of energy for the future, which has been extensively studied for the last 60 years. Already at the beginning of the fusion research, in 1955, it was stated that even with the most optimistic assumptions the conditions for the operation of a useful thermonuclear reactor will be very severe [1]. The greatest obstacle, which kept the thermonuclear reactor beyond the mankind's reach, is hidden deep within the elemental interaction of matter. The counteracting phenomenon is the Coulomb force, repulsing positively charged atomic nuclei. The repulsive forces can be overcome by increasing collisional energies of the nuclei. This can be achieved by heating up the particles to temperatures to orders of tens of thousands of electronvolts. The overall rate of fusion reactions also grows with particle density. The key parameters for the fusion energy are, thus the fuel temperature and density. Tokamaks are one of several viable approaches to so called magnetic confinement fusion. The general idea consists in high temperature plasma confinement in a magnetic field with toroidal structure generated by external electromagnetic coils. in order to explore the high temperature plasma properties while pursuing the vision of a useful thermonuclear reactor.

Reaching the break even point for energy generation requires tokamaks to confine plasmas with temperatures in orders of tens of kilo-electronvolts and particle densities of the orders of 10^{20} particles per cubic meter. Performing measurement in such conditions is extremely challenging for available diagnostic methods. Since the temperature and density play both an important part in the assessment of the plasma performance, their diagnostic is crucial. As stated above, the plasma temperature can rise up to millions of degrees Celsius, which eliminates conventional temperature measurements based on heat transmission. Spectroscopic measurements are one of possible alternatives to provide the determination of plasma temperature.

A diagnostic method based on the Thomson scattering (TS) is an essential tool for the fusion research. Not only it can provide simultaneous measurements of electron temperature and density, but it does so across the whole plasma profile without perturbing it. The demands on the diagnostics performance and precision are very high in many aspects. Principally, the cross-section of TS process is very low, this sets

the level of useful signal leaving the plasma region to be usually in order of hundreds of photons. Therefore, extremely sensitive detection apparatus must be integrated together with tools for mitigation of ubiquitous broadband background radiation and stray light, which can decrease the reliability of the diagnostic. Consequently, maintaining a precise alignment and performing a complete set of calibration routines are indispensable to be implemented to suppress any gratuitous losses of useful signal.

The overall intention of this thesis is to analyse and implement a new data processing system accompanied by novel methods extending the calibration process. Both assignments are supposed to lead to enhancing the diagnostic performance and improving its precision, accuracy and reliability. In order to understand the TS diagnostic properly Part I is devoted to both theoretical basics and its realization. Chapter 2 of this thesis is dedicated to the relevant plasma physics necessary to understand the nature of plasma as a scattering medium. The principles of relevant processes, namely Thomson, Raman and Rayleigh scattering, are summarized and the relevant equations and quantities are given. To illustrate the implementation of a diagnostic system based on Thomson scattering, the TS on the COMPASS tokamak is described in chapter 3. Major effort is devoted to the description of crucial components with emphasis on those discussed afterwards in the text.

In Part II of this thesis the author's contributions are described. In chapter 4, an extensive effort is devoted mainly to the data processing system as it is the major task in the assignment of the thesis. The author's intention is to present the whole process from the beginning, when the raw data are collected, to the final stage when the electron temperature and density is determined. Firstly, the data processing algorithm is analysed and partial segments are distinguished and visualized to be described individually afterwards. Secondly, particular calibration routines are introduced. Absolute and spatial calibration, which require author's implementation, are studied more in detail. Finally, the method for determination desired plasma parameters from the measured signal is presented. The process of incorporating all partial results of calibrations is described step by step to achieve reasonable comprehensibility. The last chapter of the thesis, chapter 5, is devoted to the exploitation and optimization of the spatial calibration method called "split-fibre". Results and advancements obtained within the last chapter were presented at 22nd Topical Conference on High Temperature Plasma Diagnostics in April 2018 and the manuscript was handed over for the submission process in May 2018.

Part I

Theoretical and experimental background

Chapter 2

Theoretical part

Present day thermonuclear fusion research is closely associated with exploration of plasma physics and its behaviour in diverse conditions. Therefore, following chapter is concerned with theoretical basics of plasma physics and processes which are relevant to the related topic of scattering of electromagnetic radiation, namely Rayleigh, Raman and Thomson scattering. Elemental statements defining plasma nature and behaviour are given and detailed features and processes based on previous assumptions are described below. Plasma conditions inside experimental devices are presented in order to highlight the key aspects that have to be considered to perform reliable measurement and diagnostics.

Having described basic plasma physics, theory of Thomson scattering itself is covered in the section 2.2. Principles of the mentioned the phenomenon are supplemented by equations predicting essential characteristics of scattered radiation, i.e. power and spectral properties. Presented results ensure the possibility for this type of diagnostic, due to the fact that the character of scattered light reflects plasma parameters, specifically the temperature and density.

2.1 Basic plasma physics

As the temperature of a material raises, its state changes from solid to liquid, then from liquid to gas. If the temperature increases even higher, certain amount of atoms become ionized. Plasma cannot be referred to as any ionized gas, because each gaseous medium shows certain degree of ionization. Even the surrounding ambient air is partly ionized by a cosmic radiation. Therefore plasma is defined as a *quasi-neutral medium with free charge carriers that behaves collectively* [2].

2.1.1 Plasma behaviour

The quasi-neutrality is a characteristic feature of a certain volume, which in average shows on a microscopic scale the same quantity of positive and negative charges, but when observed as a whole from the outside on a macroscopic scale acts as neutral. As stated before, plasma consists of free charge carriers and consequently is conductive and reacts on a magnetic or electric field. This implies that plasma can be shape and

confined by external magnetic field. his consequently brings undesirable effects, for instance drifts, waves and instabilities.

The third mentioned property was the collective behaviour of plasma. Moving charged particles generate electromagnetic field which alters the motion of other charged particles present in plasma. The thermal motion of particles may cause local perturbations of plasma density or potential, which induce electric field that can affect plasma on relatively long distances compared to those between two particles. As a result, plasma is a system of charged particles that generate fields to which the plasma reacts in turn.

The term quasi-neutrality is closely related to the Debye shielding, the fundamental phenomenon of plasma which is responsible for the neutrality on a macroscopic scale. Shielding mechanism can be described on a situation when a free test charge is placed to the plasma environment. Charged particles interact strongly by means of the Coulomb force[1] proportional to $1/r$, where r represents the relative distance between particles. For most plasmas the electron n_e and ion n_i concentration has the Boltzmann distribution in a potential ϕ given by following equation

$$n_{\mathrm{e,i}} = n_0 \exp\left(-\frac{q_{\mathrm{e,i}}\phi}{k_\mathrm{B} T_{\mathrm{e,i}}}\right), \tag{2.1}$$

where q, n_0, T refer, respectively, to particle charge and unperturbed plasma density and temperature. k_B is the Boltzmann constant and indices i and e denote ions and electrons, respectively. Charges with opposite signs are drawn towards each other and those with the same signs are driven away. Thereby, its potential is reduced or in other words shielded. The shielding is applied regardless of the sign of charge of the test particle, thus let us assume a positive charge carrier. Negatively charged particles are attracted to the test charge whereas positive are repulsed causing the plasma polarization. Using the Poisson equation one can derive generated electrostatic force which exponentially decreases the potential of the test charge. Considering single ionized hot plasma ($n_\mathrm{e} = n_\mathrm{i}$, $q_\mathrm{e} = -e$, $q_\mathrm{i} = e$, $T_\mathrm{e} \gg T_\mathrm{i}$) shielded potential ϕ as a function of r can be written as

$$\phi(r) = \frac{q_{\mathrm{e,i}}}{4\pi\varepsilon_0}\frac{\exp(-r/\lambda_\mathrm{D})}{r} \qquad \lambda_\mathrm{D} = \left(\frac{\varepsilon_0 k_\mathrm{B} T_\mathrm{e}}{n_\mathrm{e} e^2}\right)^{1/2}, \tag{2.2}$$

where ε_0 represents the vacuum permittivity. The characteristic distance λ_D of described phenomenon is called the Debye shielding length, which has a major role in plasma physics. Let us assume L as the characteristic dimension of certain plasma volume. Then if the condition $L \gg \lambda_\mathrm{D}$ is satisfied the plasma is considered to be neutral in charge. On the contrary, if $L < \lambda_\mathrm{D}$ individual particles are not fully shielded and is more precisely described by an assembly of independent or partly shielded charged particles. In general, Debye length states the characteristic distance for mutual particle interaction.

Plasma frequency is a result of the collective behaviour. A brief derivation is given below. Let us consider the case where small perturbations occur in other-

[1] The Coulomb force is a long-range force, on short distances particles interact by means of *nuclear forces*, which are neglected in this case.

wise uniform plasma. Ions are approximately three orders of magnitude heavier than electrons, thus, will be assumed stationary in relation to the electron motion. Nonuniformities in electron density generate non zero local electric charges and consequently electric fields. Induced field accelerates electrons in the direction to balance the perturbation in order to suppress the disequilibrium. The described acceleration and electron inertia lead to oscillations with characteristic frequency ω_p. It is called electron plasma frequency and is defined as 2.3, where n_0, e and m_e represent initial electron density, electron charge and mass, respectively; ε_0 refers to vacuum permittivity [2, p.8].

$$\omega_p^2 = \frac{n_0 e^2}{\varepsilon_0 m_e} \tag{2.3}$$

Electron plasma waves have this exact frequency and are the basic demonstrations of the collective behaviour of plasma. Plasma is a medium that requires much more complex and sophisticated approach in order to describe other features, including other types of waves, drifts, plasma stability and instability, or transport mechanisms. Their description is out of the extent of this work but could be found in [2, 3], [4, czech only].

Unique behaviour and extraordinary phenomena have been making plasma highly attractive object of physical and engineering research for more than one hundred years since its discovery in 1879 by Crookes [5].

2.1.2 Plasma waves

In this section the characteristic behaviour of plasma related to the topic of this thesis concerning interaction with waves in the plasma is described. The generation and propagation of waves in the plasma represent its typical phenomena, which may drive the motion of particles within the plasma. Stated above, the most typical phenomenon reflecting plasma reaction to external interference occurs with electron plasma frequency (2.3).

When describing waves in plasma, it is assumed that plasma is comprised from several fluids of different types of charged particles, e.g. electron fluid, ion fluid. This approach is called fluid dynamics. Initial set of equations is based on conservation laws (mass, momentum, energy) usually in the form of partial differential equation (PDE). If necessary, additional equations for fields or forces are added and the set is typically enclosed by an appropriate equation of state [4]. Due to the non-linear character of equations linearisation method together with Fourier transformation are ordinarily used in order to acquire approximate results or typical features of the system, e.g. dispersion relation[2], formula for refractive index, condition of resonance or stability etc.

Plasma oscillations and waves, acoustic and electromagnetic waves could be derived following the outlined method. For the future purposes table of dispersion relations of mentioned phenomena is included, see Tab. 2.1. Relative direction of

[2]Relation between wave angular frequency ω and size of wave vector $\vec{k}$ for a wave propagating through space as $\exp(i\vec{x}\cdot\vec{k} - i\omega)$.

wave propagation to the orientation of external magnetic field $\vec{B}$ is noted if necessary, because magnetic field brings anisotropy to the system.

Wave type	Formula		Condition
Plasma oscillations	$\omega^2 = \omega_{p_e}^2 + \omega_{p_i}^2$		-
Plasma waves	$\omega^2 = \omega_{p_e}^2 + c_e^2 k^2$		$m_i \to \infty$
Acoustic (ion) waves	$\omega^2 = \omega_{p_i}^2 \left(1 + \gamma_i \lambda_{D_i}^2 k^2 - \frac{1}{1+\gamma_e \lambda_{D_e}^2 k^2}\right)$		$m_e \to 0$
Electromagnetic wave complex			
R wave	$\vec{k} \parallel \vec{B}$	$N_R^2 = 1 - \frac{\omega_p^2/\omega^2}{1-\omega_c/\omega}$	
L wave	$\vec{k} \parallel \vec{B}$	$N_L^2 = 1 - \frac{\omega_p^2/\omega^2}{1+\omega_c/\omega}$	$m_i \to \infty$
O wave	$\vec{k} \perp \vec{B}$	$N_O^2 = 1 - \frac{\omega_p^2}{\omega^2}$	$p \to 0$
X wave	$\vec{k} \perp \vec{B}$	$N_X^2 = 1 - \frac{\omega_p^2}{\omega^2} \frac{\omega^2 - \omega_p^2}{\omega^2 - \omega_p^2 - \omega_c^2}$	

Tab. 2.1: Dispersion relation or refractive index N formula for different kinds of waves in plasma. Various mentioned quantities are defined above, see (2.2), (2.3), ω_c refers to the cyclotron frequency of given type of particle, N represents refractive index defined as $N = ck/\omega$ and p signifies pressure. [4, 2]

Adding equations for magnetic field to standard fluid dynamics results in a new way of describing plasma - *magnetohydrodynamics* (MHD), which is possible to use for derivation of additional types of waves produced and transmitted by plasma, e.g. Alfvén or magnetoacoustic waves [2, p. 46].

2.1.3 Plasma conditions in tokamaks

Plasma is a very complex medium with many interesting but complicated properties which makes plasma attractive for scientists. Furthermore understanding and mastering of plasma is assumed to be crucial for achieving sustainable source of energy from thermonuclear fusion in the future. This fact raises the attention even more and it is one of the reasons for a great development in plasma and fusion physics since 1950s.

Majority of current fusion[3] research projects is aimed at the thermonuclear approach, when the sufficient amount of energy-emerging reactions is achieved using high temperatures.

In general, the fundamental endeavour of thermonuclear fusion research is to

[3] *fusion* - in the sense of nuclear fusion, a reaction in which two or more atomic nuclei come close enough to form one or more different atomic nuclei and subatomic particles.

achieve high values of plasma parameters, temperature and density, and its containment in that ideally stable situation as long as possible. Plasma parameters sufficient for thermonuclear fusion process are given by Lawson criterion 2.4, which states the fundamental condition for achieving sustainable thermonuclear source of energy. Quantities n,T and τ_E represent plasma density, temperature and the confinement time of stored energy, respectively, defined in the same equation as a ratio of plasma energy W_p and power of loses P_L, respectively. The expression following the equal sign refers to the most convenient yet not the ideal fusion reaction between deuterium **D** and tritium **T**.

$$n\tau_E \geq f(T) = \frac{60 k_\mathrm{B} T}{\varepsilon_f < \sigma v >} \qquad \tau_E = \frac{W_\mathrm{p}}{P_\mathrm{L}} \tag{2.4}$$

On the basis of this criterion Lawson already in 1955 stated:

"Even with the most optimistic possible assumptions it is evident that the conditions for the operation of a useful thermonuclear reactor are very severe". [1]

Two principal approaches (and several variations of them) trying to cope with the Lawson criterion requirements emerged, namely inertial (ICF) and magnetic confinement fusion (MCF) are the two ways. For the purposes of this work only the MCF is briefly described. Tokamak device, as a leading concept in the thermonuclear fusion research in general, is based on the confinement of plasma with magnetic fields. When high currents are applied on several types of magnetic coils, the strong external magnetic field is created in the shape of a torus, therefore, a vessel for plasma confinement is toroidal. Folding together with the magnetic field produced by electric current flowing through the plasma, once is created within the tokamak vessel, results in theoretically stable helical field structure.

Once a discharge is initiated, plasma becomes controlled, shaped, heated and otherwise affected in order to reach specific experimental goals. Typical range of values of key parameters during standard operation of various tokamak devices around the world, including the COMPASS tokamak, is summarised in Tab. 2.2.

Parameter ╲ Device	**COMPASS**	**ASDEX-U**	**JET**	**ITER**
B_T [T]	0.9 - 2.1	3.9	3.5	11.8
I_p [MA]	0.4	2.0	3.2 - 4.6	15.0
t_d [s]	1	10	20	60 - 3600
n_e [10^{20} m^{-3}]	0.8	2.0	1.5	1.1
T_e [keV]	2	10	10	15
ω_p^2 [10^{23} s^{-2}]	2.545	6.364	4.773	3.500

Tab. 2.2: Table of operation values of various parameters when operated given tokamak in a standard mode, where B_T, I_p and t_d refers to amplitude of toroidal magnetic field, plasma current at maximum and discharge length and n_e, T_e and ω_p represents electron density and temperature and plasma frequency, respectively. [6, 7, 8, 9]

Electron temperature is given in energy units (eV), typical units for plasma physics which correspond to the energy of the thermal motion. The electron temperature will be exclusively expressed in eV through the entire thesis.

2.2 General theory of Thomson scattering

The Thomson scattering, firstly described by Nobel prize laureate J. J. Thomson, is the scattering of electromagnetic radiation by a free charged particle in a low energy limit. By classical physics the process is described as the acceleration of a free charged particle by the electric field component of an incident wave and the subsequent re-radiation of electromagnetic radiation by the charged particle into other directions [10, p. 2]. Process is schematically pictured in Fig. 2.1. The incident wave approaches free charge particle which becomes accelerated by its electrical field and starts to emit the radiation, thus, creating the scattered wave propagating isotropically.

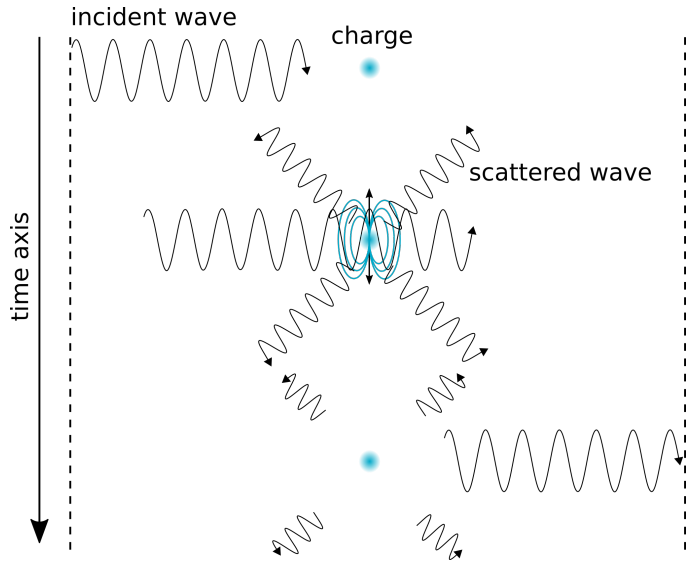

Fig. 2.1: The scheme of the process of scattering by a free charged particle, inspiration [11, p. 8].

The diagnostic system based on the Thomson scattering is a very powerful and non-perturbing technique used in plasma physics research, which provides detailed information about electron (ion) temperature and density. As stated below, the Thomson scattering cross-section is very low, thus high-intensity monochromatic light sources (Q-switched lasers) are indispensable in order to achieve sufficient production of scattered radiation.

An electromagnetic wave travels through the plasma respecting the dispersion relation presented in previous section in Tab. 2.1. Laser generated linearly polarized propagating perpendicularly to the magnetic field lines, used as a probing beam on COMPASS TS, behaves in the plasma as the ordinary wave (O wave). The ratio ω_p^2/ω^2 can be evaluated using the parameters from Tab. 2.2 and the laser wavelength

$\lambda_L = 1064$ nm, which yields to $\omega_p^2 \approx 2.5 \cdot 10^{23} s^{-2}$ and $\omega^2 \approx 3.14 \cdot 10^{30} s^{-2}$. Values are orders of magnitude different and condition $\omega_p^2 \ll \omega^2$ is clearly satisfied, thus, the refractive index N_O is unity and the wave propagates through the plasma unchanged. Same relation is obtained if the angular frequency of the laser is compared to the electron cyclotron frequency. In conclusion, the laser beam travels through the scattering region as if there is no plasma.

2.2.1 Thomson scattering process

Following subsection will describe the process of Thomson scattering. As mentioned before it is based on wave-particle interaction. From this point on, only electron induced Thomson scattering will be discussed. Similar derivations might be done for the one induced by ions, but, as stated below, ion scattering is orders of magnitude less significant. Incident electromagnetic (EM) wave accelerates a free charged particle, electron, which experience the radiation at a different frequency due to Doppler effect, as a result of the electron's relative motion to the EM source with non-zero velocity. Accelerated electrons emit radiation, which is also Doppler shifted, due to the relative motion of the electron to the observer. Therefore scattered spectrum is shifted twice. Diagnostic system objective is to measure the scattered radiation. The magnitude of the shift reflects information about electron temperature T_e, whilst the measured intensity is proportional to electron density n_e. Typical temperatures achieved in plasma experimental devices range from units of eV to tens of keV.

Thomson scattering geometry and cross-section

From the calculation of radiated power of scattered light one can determine Thomson scattering *cross-section*, which has a relation to the probability of single scattering event. In general directional energy flux density of an electromagnetic field is represented by Poynting vector where the electric field generated by a moving charged particle is substituted. This field one can determine from Lienard-Wiechert potentials [10, p. 5]. Total radiated power is defined as the energy over time integrated over whole sphere. Carrying out the integration results in the equation (2.5), where q represents charge of the particle (electron charge) and $\gamma = 1/\sqrt{1-\beta^2}$, where $\vec{\beta} = \vec{v}/c$, remaining quantities can be recognized from Fig. 2.2a or defined above. Fig. 2.2a shows the scattering coordinate system. Light scattered by *particle* with the $\vec{v}$ speed at the *origin* is observed by the *observer*. Vector $\dot{\vec{\beta}}$ refers to the acceleration of the particle given by the electric field $\vec{E}_i$ of the incident electromagnetic wave.

$$P_{tot} = \frac{q^2\gamma^6}{6\pi c\varepsilon_0}\left[\dot{\beta}^2 - \left(\vec{\beta}\times\dot{\vec{\beta}}\right)^2\right] \tag{2.5}$$

Strong dependence on the γ factor indicates that an accelerated charged particle radiates strongly as its speed rises. Two basic situations can be distinguished depending on the orientation of vectors $\vec{\beta}$ and $\dot{\vec{\beta}}$. In both cases the accelerated particle emit in the direction of $\vec{\beta}$ more and more as its speed approaches the speed of light,

referred to as *headlight effect*. High-speed electrons from the velocity distribution thus scatter more light in their motion direction, i.e. towards an observer. Electrons moving away from the observer will scatter very little portion of light in the direction of the observer. Consequently combination of these two effects will due to Doppler effect shift the peak of the spectrum of the scattered light towards the shorter wavelength, so called *blue-shift*. More information and detailed derivation of mentioned facts together with visualisation could be found in [10].

The Thomson scattering cross section σ_{TS} is typically derived for low-temperature case when $\beta \ll 1$, $\gamma \equiv 1$. The total radiated power P_{tot} of the Thomson scattering is then given as:

$$(a) \quad P_{tot} = \frac{8\pi}{3} r_e^2 S_{inc} \qquad (b) \quad r_e = \frac{e^2}{4\pi\varepsilon_0 m_{0e} c^2} \tag{2.6}$$

where the quantity r_e is known as standard electron radius and S_{inc} denotes to the magnitude of the instantaneous Poynting vector. The quantity of proportion between P_{tot} and S_{inc} is called Thomson scattering cross section σ_{TS} (2.7a) and it is very small, equal to $6.65\times10^{-29}\mathrm{m}^2$. As a consequence only high intensity light sources enable using this diagnostic technique. Also σ_{TS} is inversely proportional to particle's mass squared, therefore, an electron scatter approximately 3.4×10^6 more power than an ion under the same conditions [10, p. 14]. This makes the Thomson scattering by ions negligible in contrast to the one induced by electrons.

$$(a) \quad \sigma_{TS} = \frac{8\pi}{3} r_e^2 \qquad (b) \quad \frac{d\sigma}{d\Omega} = r_e^2 \sin^2\theta_3 \tag{2.7}$$

Differential cross-section $d\sigma/d\Omega$ can be derived from equation for the power dP radiated per unit solid angle $d\Omega$ using the same approximation. The result is shown in equation (2.7b), where θ_3 is the angle between $\vec{E}_i$ and $\hat{s}$ from the Fig. 2.2b. Differential cross sections shows the spatial distribution of scattered power. It is maximal when $\theta_3 = 90°$. Thomson scattering is therefore most effective in the plane perpendicular to $\vec{\beta}$, in other words in the plane of the polarization of the incident

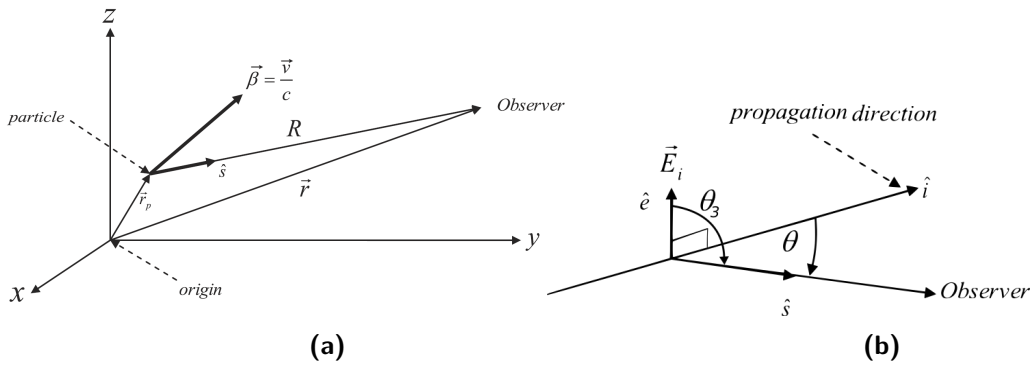

Fig. 2.2: (a) Diagram showing the scattering coordinate system, (b) The incident electric field $\vec{E}_i$ is perpendicular to the scattering plane defined by unit vectors $\hat{s}$ and $\hat{i}$ [10]

electromagnetic wave. Therefore polarizers are often used to select the desired polarization to ensure the highest efficiency of the diagnostic. For most cases linear polarization of the probing laser is used.

Spectrum of the scattered light

Last section is denoted to the derivation and discussion the spectrum of the scattered light. One can determine the spectrum from the scattering of incident wave by a single electron, which is afterwards averaged over the ensemble of particles with characteristic velocity distribution. Stated before the scattering process strongly depends on particle (electron) velocity and considering that the particle energy within the high-temperature plasma might reach substantial portion of the speed of light, Maxwell-Boltzmann velocity distribution is modified to take account the relativistic effects[10, p. 43]. In this case, the relativistic formula for the velocity distribution function is

$$f_{\mathrm{R}}(\vec{\beta}) = \frac{\alpha}{2\pi K_2(2\alpha)} \frac{\exp\left(-2\alpha(1-\beta^2)^{-\frac{1}{2}}\right)}{(1-\beta^2)^{\frac{5}{2}}}, \tag{2.8}$$

where $\vec{\beta} = \vec{v}/c$ for speed of the electron $\vec{v}$, $K_2(2\alpha)$ is the modified Bessel function of the second order and second kind and parameter $\alpha = m_0c^2/2k_{\mathrm{B}}T$, where m_0c^2 is the rest mass of an electron, k_{B} in Boltzmann's constant and T is the temperature in Kelvin. [10]

Spectral function S giving the spectral distribution of the scattered radiation by a set of particles with chosen velocity distribution can be determined evaluating following integral

$$S = \int\int\int \left(\frac{\omega_{\mathrm{s}}}{\omega_{\mathrm{i}}}\right)^2 (1-\beta^2)\, f_{\mathrm{R}}\left(\vec{\beta}\right) \delta\left(\vec{k}\cdot\vec{v}-\omega\right) q(\vec{\beta}) \mathrm{d}^3\vec{\beta}, \tag{2.9}$$

where ω_{s} and ω_{i} represents the angular frequency of scattered and incident (laser) light wave, respectively, and δ refers to the Dirac delta function. The quantity q represents the so-called *depolarization term* defined as

$$q = \left[1 - \frac{\beta_{\mathrm{e}}^2(1-\hat{s}\cdot\hat{i})}{(1-\beta_{\mathrm{i}})(1-\beta_{\mathrm{s}})}\right]^2, \tag{2.10}$$

where β_e, β_i and β_s stands for the projection of $\vec{\beta}$ into the direction of electric field of the incident wave $\hat{e}$, its propagation direction $\hat{i}$ and scattering direction $\hat{s}$ (see Fig. 2.2), respectively. Due to the depolarization the orientation of the electric field vector of the incident radiation as seen by the moving electron [10]. This effectively changes the polarization of the scattered wave.

In the following part the integration (2.9) is carried out, for the case when the depolarization is neglected. It can be done due to the fact, that its effect does not alter the shape of the spectrum in relevant wavelength range and the reduction of intensity is not negligible only once the temperatures of 10 keV are exceeded. For

illustration the Fig. 2.3(bottom) shows the dependency of depolarization term on temperature for standard TS configuration. It can be observed that for $T_e = 20$keV the intensity reduction is approximately 7% and remains constant in the relevant wavelength range from 500 to 2000 nm, while for temperatures below 5 keV remains under 2%.

Carrying out the integration for this situation results in the term (2.11). Previously not described quantities α, ε and x are given by (2.12), where λ_s and λ_i stands for wavelength of the scattered and incident (laser) light and angle θ is defined in Fig. 2.2b.

$$S(\varepsilon,\theta,2\alpha) = \frac{\exp(-2\alpha x)}{2K_2(2\alpha)(1+\varepsilon)^3}\left[2(1-\cos\theta)(1+\varepsilon)+\varepsilon^2\right]^{-1/2} \tag{2.11}$$

$$\alpha = \frac{m_0c^2}{2k_BT} \qquad \varepsilon = \frac{(\lambda_s-\lambda_i)}{\lambda_i} \qquad x = \left[1+\frac{\varepsilon^2}{2(1-\cos\theta)(1+\varepsilon)}\right]^{1/2} \tag{2.12}$$

Spectral function S calculated using (2.11) is shown in Fig. 2.3(top) for temperature range from 1 to 20 keV, when only electrons are considered as a scattering medium, for 90° geometry diagnostic system. Shift of the peak position to shorter wavelength with increasing temperatures (*blue-shift*) can be observed together with the broadening of the whole spectrum.

In principle, the aim of a diagnostic system based on Thomson scattering is to reconstruct the scattered spectrum from detected signal. Eventually spectrum width and shift of its peak leads to determination of electron temperature and the measured intensity is proportional to electron density.

During the reconstruction, it is reasonable and substantially faster to use approximation rather than evaluate precise spectrum. The scattered power per unit wavelength for the case of relativistic Thomson scattering, presented for instance in [12], can be written as follows

$$\begin{aligned} S(\varepsilon,\theta,\alpha) &= c(\alpha)\cdot A^{-1}(\varepsilon,\theta)\exp(-2\alpha B(\varepsilon,\theta)) \qquad (2.13)\\ \text{where}&\\ A(\varepsilon,\theta) &= (1+\varepsilon)^3\left(2(1-\cos(\theta))(1+\varepsilon)+\varepsilon^2\right)^{1/2}\\ B(\varepsilon,\theta) &= \left(1+e^2/(2(1-\cos(\theta))(1+\varepsilon))\right)^{1/2}-1\\ c(\alpha) &= (\alpha/\pi)^{1/2}\left(1-\frac{15}{16}\alpha^{-1}+\frac{345}{512}\alpha^{-2}+\ldots\right) \qquad \text{when} \quad \alpha \gg 1 \end{aligned}$$

The error of spectral density calculated using presented approximation S_{app} in comparison to the analytical function S is shown in Fig. 2.4, where the quantity $(S_{app}-S)/S$ is plotted for the same temperature range and scattering angle θ. Even for high temperatures (20 keV) the error is below 0.03%, which indicates high level of reliability of the approximation across the temperature range and justifies its application for standard analysis of TS signal.

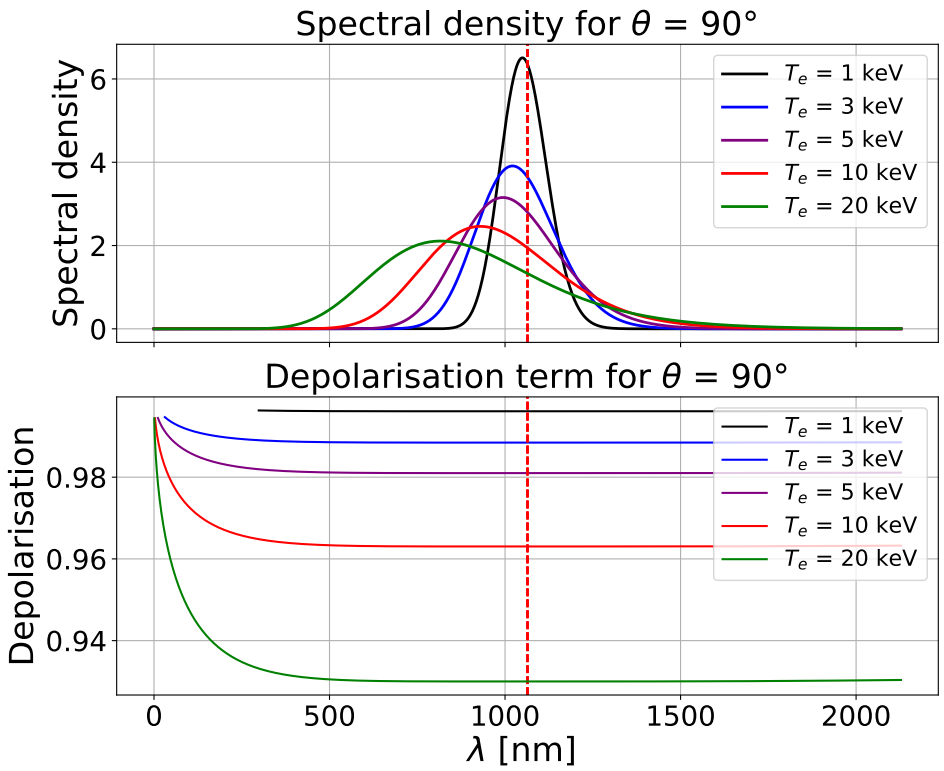

Fig. 2.3: (top) Spectrum of the scattered light S as a function of ε for temperature range 1 - 20 keV for 90° geometry TS. (bottom) The dependency of depolarization term on ε for the same parameters and geometry.

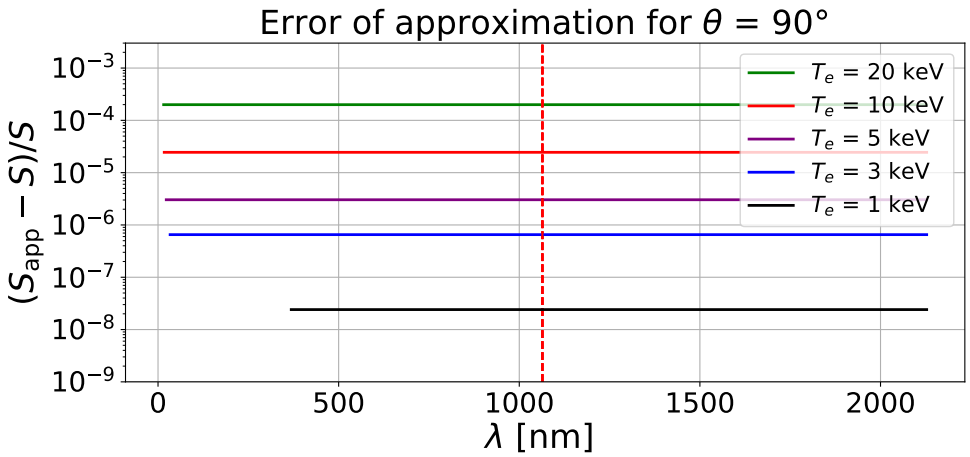

Fig. 2.4: Error of the approximation S_{app} presented in (2.14) with respect to analytical spectral density function S in (2.11).

2.3 Theory of Rayleigh and Raman scattering

When electromagnetic wave encounters with individual atoms or molecules rather than single charged particles, similar processes as Thomson scattering might occur. For the purposes of this work Rayleigh and Raman scattering are relevant and are described below.

Light scattering originates from the particle ability to form instantaneous dipoles, in other words its polarizability. The oscillating electric field of an electromagnetic wave affects the charges within a particle, which adopt an oscillation of the same frequency. The oscillation results in the periodic separation of charge inside the particle, which is called an induced dipole moment. Such oscillating electric dipole acts as a source of electromagnetic radiation. The majority of emitted light has the same frequency as the incident light wavelength, this is referred to as an elastic scattering or the Rayleigh scattering. However, a portion of light, generally orders of magnitude less than Rayleigh scattered light, is emitted with a different frequency. This case is referred to as an inelastic or Raman scattering. The frequency shift of the scattered wave is caused by an interaction with vibrational or rotational states of given particle. Both lower and higher wavelengths can be observed depending on the particle state. In this case, it is referred to as Raman anti-Stokes and Stokes scattering lines, respectively. [13]

Both Rayleigh and Raman scattering provide a possible tool to perform the absolute calibration of the Thomson scattering diagnostics, however, diagnostic implementation and used components must be compatible with the corresponding calibration method. In the case of Rayleigh scattering, signal detectors at the laser beam wavelength are required together with a high-level quality system of a laser stray light mitigation. On the other hand, employing the calibration by means of the Raman scattering is fundamentally resistant to the stray light as the relevant signal has different wavelength. Unintentional stray light radiation is effectively reduced by high magnitude suppression filters. The Rayleigh calibration is usually used for Thomson scattering systems based on ruby or different visible lasers, while the Raman anti-Stokes calibration is dominantly used when infra-red probing lasers are accommodated. [14]

2.3.1 Raman scattering

As stated above Raman scattering occurs at a number of discrete wavelengths around λ_L. The values of them and the intensities at each of them are given by the vibrational and rotational states of the molecule within the scattered medium. Generally, the frequency shift due to the vibrational state is much larger compared to the rotational one, therefore, only the latter is commonly used for the purpose of absolute calibration. Moreover, spectral transmissivity of the filters used for the signal detection are designed to detect the blue-shifted Thomson scattering spectrum, thus, only the Raman anti-Stokes lines, whose wavelength is lower than λ_L, are considered. [15, 16]

Raman scattering cross-section

The total rotational Raman cross-section (RCS) seen by a filter ρ_{Raman} may be calculated from the total contribution of the Raman line intensities $\rho_{Raman}(J)$ and filter transmissions $T(\lambda_J)$, which is measured during the spectral calibration routine, at each wavelength for each rotational state J:

$$\rho_{\mathrm{Raman}} = \Sigma \rho_{\mathrm{Raman}}(J) T(\lambda_J) \tag{2.14}$$

For the purposes of calculation of rotational Raman scattering cross-section in relevant gases, for instance N_2, O_2, H_2 or CO_2, molecules are treated as simple linear molecules, in other words linear molecules with no electric angular momentum. This approach is not precise for the case of O_2 or CO_2, but produced discrepancies are within the range of experimental precision. For such molecules, allowed transitions in rotational Raman scattering are $J \rightarrow J \pm 2$. The Raman frequency shifts to corresponding transitions are $\Delta\omega_{J\rightarrow J+2} = -(4J+6)B_0$ and $\Delta\omega_{J\rightarrow J-2} = (4J-2)B_0$, where B_0 in the rotational constant fo the lowest vibrational level [17]. Values of B_0 for various gases in summarized in Tab. 2.3. Only Raman anti-Stokes, $J \rightarrow J-2$, transitions are further considered as they are relevant as a calibration tool. Frequency shift at which the Raman anti-Stokes occurs can be written in wavelength terms as follows:

$$\lambda_J = \frac{1}{\frac{1}{\lambda_{\mathrm{L}}} + B_0(4J-2)} \tag{2.15}$$

Raman line intensities at wavelengths λ_J given by state J may be calculated from the fraction of molecules in each state $F(J)$ multiplied by their differential cross-section $S(J)$ [15].

$$\rho_{\mathrm{Raman}}(J) = F(J)S(J) \tag{2.16}$$

For a gas in thermal equilibrium at the temperature T_{gas} the distribution of fractions occupying each rotational state is given by following formula

$$F(J) = Q^{-1} g(J)(2J+1) \exp\left(-\frac{E(J)}{k_{\mathrm{B}} T_{\mathrm{gas}}}\right), \tag{2.17}$$

where $g(J)$ represents nuclear spin statistical weight characteristic for each medium. Q is the rotational partition function, determined by the normalization $\sum_{J=0}^{\infty} F(J) = 1$ [17] and $E(J)$ is the rotational energy, which is well approximated by

$$E(J) = hc\left(B_0(J(J+J)) - D_0(J(J+J))^2 + H_0(J(J+J))^3\right), \tag{2.18}$$

where D_0 and H_0 are additional rotational constants of given gas molecule [15]. Finally, the differential cross-section for anti-Stokes lines for transitions $J \rightarrow J+2$, can be written using following equation:

$$S(J) = \frac{7(2\pi)^4\gamma^2}{45\lambda_J^4} \cdot b_{J\to J-2} \tag{2.19}$$
$$b_{J\to J-2} = \frac{3J(J-1)}{2(2J+1)(2J-1)},$$

where the previously undefined quantities γ and $b_{J\to J-2}$, represents the anisotropy of the molecular-polarizability tensor and Placzek-Teller coefficient for $J \to J-2$ transition [15, 17].

Molecular parameters, which are needed to evaluate the rotational anti-Stokes Raman spectrum are expressed in Tab. 2.3.

	$g(J)$					
Gas	Even J	Odd J	B_0 [cm^{-1}]	D_0 [cm^{-1}]	H_0 [cm^{-1}]	γ^2 [cm^6]
N_2	6	3	1.9895	$5.72 \cdot 10^{-6}$	$3.7 \cdot 10^{-10}$	$0.51 \cdot 10^{-48}$
H_2	1	3	59.3392	$4.60 \cdot 10^{-2}$	$5.2 \cdot 10^{-5}$	$9.28 \cdot 10^{-52}$
D_2	6	3	29.9105	$1.13 \cdot 10^{-2}$	$3.6 \cdot 10^{-6}$	$9.00 \cdot 10^{-52}$
O_2	0	1	1.4378	$5.48 \cdot 10^{-6}$	-	$1.29 \cdot 10^{-48}$

Tab. 2.3: Molecular constants needed for the rotational anti-Stokes Raman scattering calculation. Values taken from [15, 17, 14, 18, 19]

Evaluating previous equations (2.15) - (2.20) and substituting constants from Tab. 2.3, one can calculate the rotational anti-Stokes Raman lines intensities at λ_J wavelengths, which is shown for nitrogen and oxygen in Fig. 2.5a together with spectral transmissivity of the first two detector channels. The detection and data acquisition system is described more in detail in chapter 3. For hydrogen and deuterium similar plot is shown in Fig. 2.5b, with spectral transmissivity of third and fourth filter. Both nitrogen and oxygen are possible to be used as a scattering medium as the shifted lines overlap with the first two spectral filters of the detector. In principle, also Raman scattering by hydrogen and deuterium molecules can provide the source of scattered light, however, it has by three orders of magnitude lower cross-section. Present-day tokamak plasma diagnostics based on Thomson scattering, including the COMPASS TS, are using nitrogen as the scattering gas, due to its lowest cost and compatibility with the vessel material.

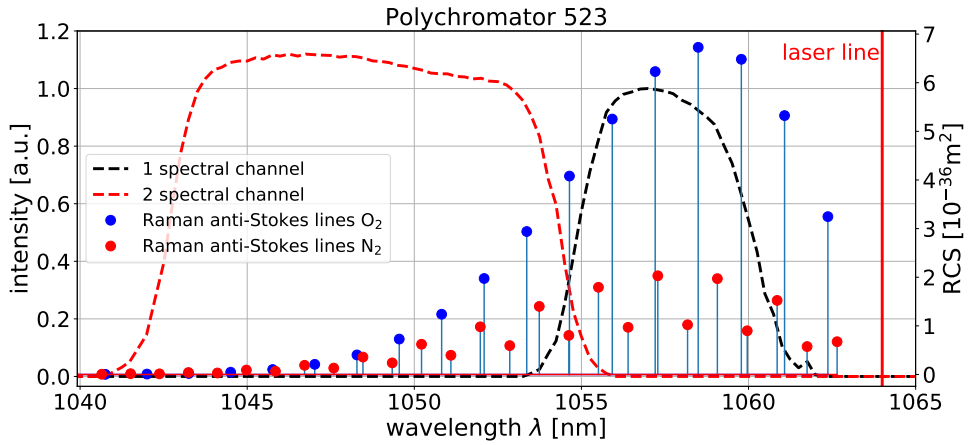

(a) Raman cross-section (RCS) calculated for N_2 and O_2.

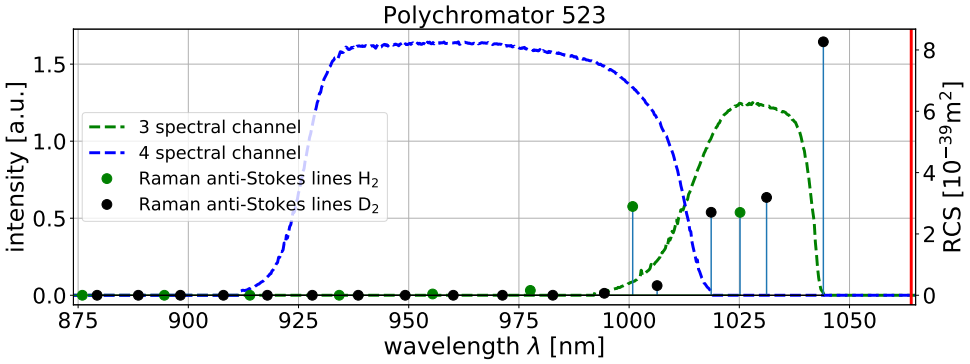

(b) Raman cross-section (RCS) calculated for H_2 and D_2.

Fig. 2.5: Rotational anti-Stokes Raman scattering cross-section. Plotted with the spectral transmissivity of the first two (a) and third and fourth (b) spectral channels. Laser line is represented by the red vertical line.

Chapter 3

Thomson scattering diagnostic system on tokamak COMPASS

In general, it can be established that the diagnostic system based on the Thomson scattering is a very complex and complicated diagnostics susceptible to even delicate spatial or temporal inaccuracy. Due to the very low cross-section (2.7) value of the TS phenomenon, TS diagnostics system becomes feasible once high-energy and high-power lasers as sources for probing electromagnetic wave are used. Despite this fact, low level intensity of scattered radiation is available, which implies very high and strict requirements on components for light collection, transmission and detection. Appropriate configuration and precise adjustment of components together with high precision calibration routines are essential to provide reliable measurement of desired plasma parameters.

The Thomson scattering diagnostic (TS) system on the COMPASS tokamak is designed to measure the electron temperature in the range from 10 eV to 10 keV and the electron density of optimally 10^{19} m^{-3}. The whole system is presented on the schematic figure Fig. 3.1, where the key components are shown, namely the lasers, the collection and transmission optics, the detectors and the data acquisition part. Following section is dedicated to mentioned components in more detailed.

3.1 Laser system

For the purposes of obtaining sufficient signal of scattered light, four independent high-power Nd:YAG lasers with the energy 1.5 J each and the repetition rate of 30 Hz are installed at the COMPASS tokamak facility. Three different regimes of laser operation are implemented. Individual control enables triggering lasers both simultaneously in order to deliver up to fourfold higher energy in a single moment and separately resulting in either 120 Hz pulse frequency or an operation in so called *"burst regime"*, when the delay between consequent pulses can be set individually and optimised for the purposes of experimental demands.

All laser beams are led to the tokamak device by an approximately 20 m long enclosed path and enter the tokamak vessel through a vacuum window placed at Brewster angle to avoid unintentional reflections. After leaving the plasma region remaining laser energy is absorbed by the laser beam dump situated 2.48 m beneath

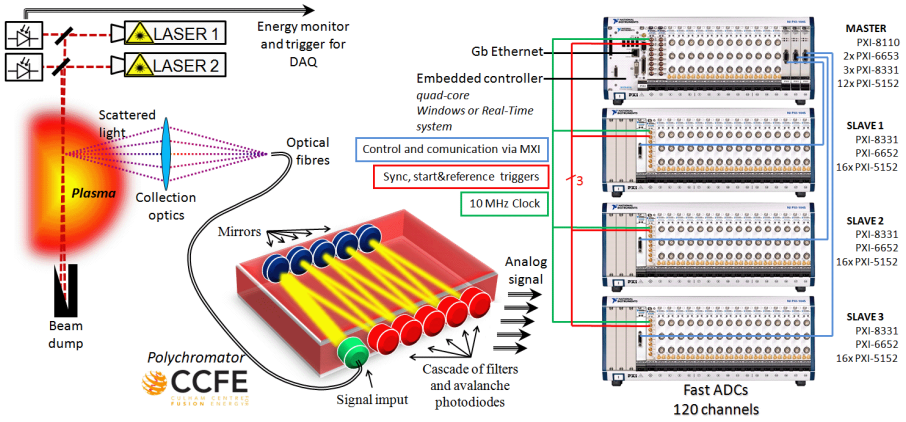

Fig. 3.1: Thomson scattering diagnostics scheme on tokamak COMPASS [6].

the vessel to prevent undesirable back reflections of laser pulses. In addition, several diaphragms are placed in the laser beam path both before and after laser beam crosses the plasma region to achieve high stray light mitigation, which is a key issue for the TS diagnostics. Optical elements, which participate in scattered light collection and transmission, are coated with the anti-reflex layer, which improves the stray light mitigation. Moreover, the inner side of the laser beam path pipe is blackened, in order to reduce its reflectivity. Additional portion of stray light that comes from plasma background as a result of bremsstrahlung is reduced by the factor of two by a polariser placed within the collection lens. Last but not least, stray light is extensively mitigated from the signal by placing a filter at the laser wavelength before it reaches the first interference filter of the polychromator. [20]

3.2 Optical system

The TS system is designed to view both the plasma edge and core region with two collection lenses optimized for respective spectral range. The area observed by the core and edge lens is pictured on Fig. 3.2, together with magnetic surfaces at specific time during the discharge number 15978. The core lens observes centre and upper part of plasma along the vertical axis from -15 mm to 213 mm over the mid-plane, with spatial resolution of 9 to 12 mm. Edge system underwent a recent upgrade during which the edge tokamak port was cut and replaced by more suitable one to facilitate the view on the edge plasma region. New collection lens was designed to accommodate and fully exploit the new port. The upgrades expanded the edge TS field of view to 215 to 32 22 mm over mid-plane with spatial resolution of 3.6 to 3.8 mm. [21]

The scattered light is afterwards focused on transmission fibre bundles, which are matched to observe defined spatial points inside the tokamak vessel. In total, the observable region is divided into 54 points, from which 24 belong to the core TS while the rest to the edge TS. Optical fibres made of polymer-clad silica are

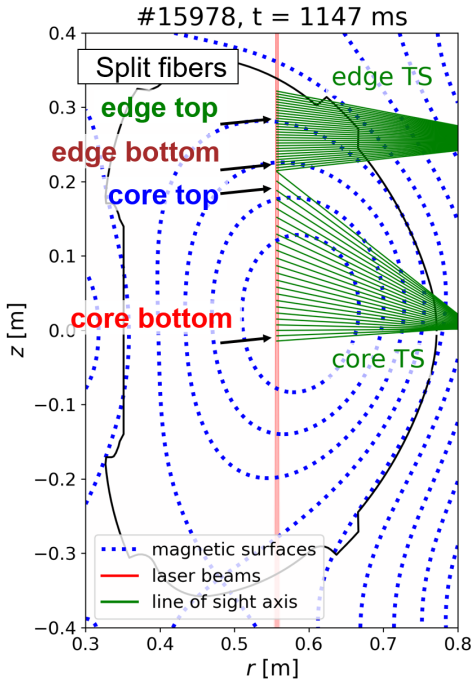

Fig. 3.2: Observed plasma region by both core and edge TS diagnostic [21]

chosen due to favourable properties when operating with infra-red part of spectrum of electromagnetic radiation. Scattered light from two adjacent spatial points is led to one detection unit (described below) by fibres of a different length, thus, enabling reduction of detection units by a factor of two. This method, so called *duplexing*, is based on a time delay of arrival of the collected signal, due to the different length of path to travel from a source to the detector.

Furthermore, several fibre bundles (2 core, 2 edge), called *"split-fibres"*, have an additional function, which helps verifying correctness of measurement. Signal from one spatial point is focused on the specific fibre bundle, which is vertically separated into halves. Then the scattered light is led to a single detector using the duplexing method, and the intensity in both halves is compared to each other. The split-fibre method is used to control relative position of the probing laser beam and collection optics. One can easily observe that ideally the ratio of intensities equals to unity. In order to use split-fibres to measure plasma parameters, signal in both halves is added together and can be used for the standard measurements. Therefore one detection unit is necessary for one split-fibre in contrast to other fibre bundles, where one detector is able to acquire data from two fibre bundles, thus two spatial points. Typical result of split-fibre measurements is shown in Fig. 3.3. The time evolution of signal intensities from the core and edge split-fibres are shown in the left and right plots on the side, respectively, during the tokamak discharge number 15978. The signal from one (left) half is presented as positive, while the other (right) half is presented as negative intensity. The time evolution of the ratio of these intensities is shown in logarithmic scale in the middle graph. One can see that in the initial and last phases of the discharge, which starts at 960 ms, the ratio in the core split-fibres

reaches larger values, which signifies larger relative movement of the laser beam and the collection optics. In the middle phase of the discharge, approximately at 1080 - 1220 ms, the ratio oscillates around the optimal value.

In addition, it was found that the time evolution of the split-fibre ratios has similar character for different discharges. This is illustrated in the Fig. 3.4 for five tokamak discharges within one experimental campaign when the main parameters were maintained. The strong correlation is apparent primarily in the core TS (two figures on the left). This suggest that the beam movement along the set of fibres is being systematically influenced by an unknown phenomenon. Searching for the origin and possible mitigation of this undesirable effect is currently in progress.

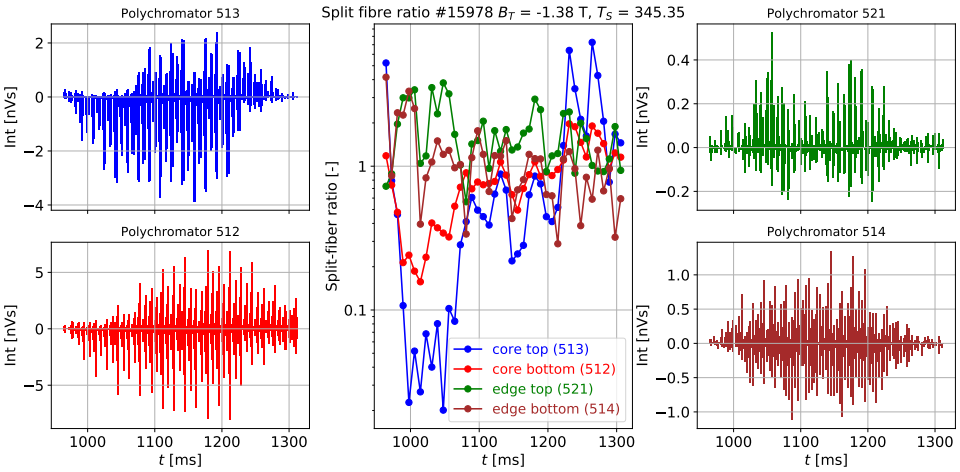

Fig. 3.3: Results from the split-fibre measurement for tokamak discharge #15978 on COMPASS, labels "bottom" and "top" signifies position inside the tokamak vessel of given spatial point for the core and edge system. Parameters B_T and T_S represents absolute value of toroidal magnetic field and the duration of the discharge, respectively.

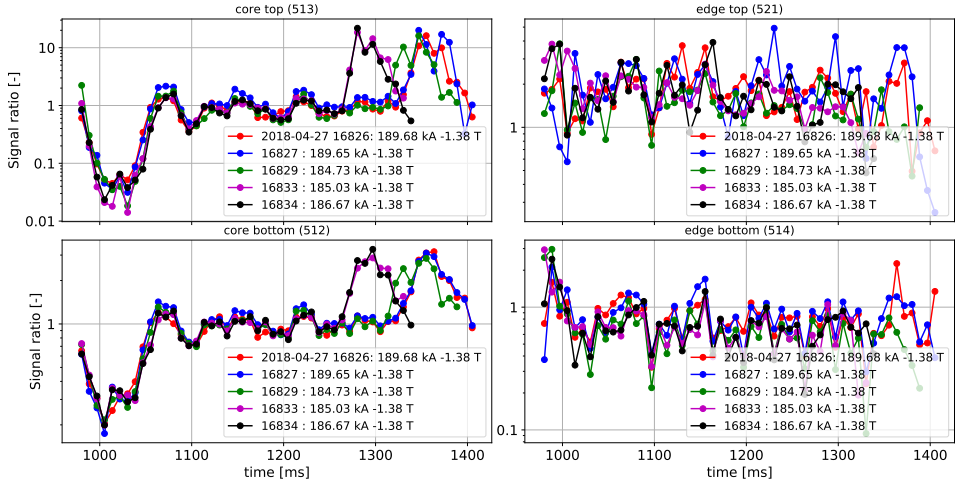

Fig. 3.4: Split-fibre ratios measured during five tokamak discharges (#16826-#16834) within one experimental campaign.

The subject of investigating results from the split-fibre method, with emphasis on mentioned phenomena, and the process of optimization of the split-fibre arrangement has recently undergone significant research by the author of this work and is presented in 5 within this thesis. This work was presented also as a contribution at 22nd Topical Conference on High Temperature Plasma Diagnostics in April 2018 and the manuscript was handed over to the submission process in May 2018.

3.3 Detection and data acquisition

Detection of spectral composition of scattered light collected by optical system is on the COMPASS tokamak provided by means of 29 filter polychromators, which are the fourth generation detectors for the purpose of TS diagnostics developed on tokamak MAST, CCFE, UK [22, 23]. Generally, the filter polychromator is a type of detector that enables the spectral decomposition of incoming optical signal. Fig. 3.5a shows the basic scheme of a polychromator model with seven filters. Input signal is reflected of the first interference filter, which transmits certain narrow spectral range, while the rest is reflected on the second filter, and so forth. Therefore, each interference filter acquires different spectral range of the input signal, which is after passing through multiplied and detected by avalanche photodiodes (APD) to obtain sufficiently high signal. The set of spectral filters, or channels, is designed in order to cover required wavelength range and to suppress unnecessary losses of the useful signal. Modified version of the pictured polychromator with five channels is integrated into the TS system on the COMPASS tokamak. The spectral transmissivity of individual filters is presented in Fig. 3.5b, where one can easily observe the covered range of wavelength with overlaps of filter transmittance to reduce potential losses.

Amplified signal leaving the APD is eventually digitized by the total amount of 120 ADC[1] converters, whose set up is illustrated at Fig. 3.1 as Fast ADCs. The digital output signal is acquired with the sampling frequency of 1GS/s in the scale of 8bits and afterwards saved and stored for following data processing and analysis. High-pass filter is used for background radiation reduction. [24]

3.4 Data processing

The overall objective of the data processing system is to reconstruct the spectrum of the scattered light from the collected signal by means of previously discussed components, in order to determine desired plasma parameters, the electron temperature T_e and density n_e. The methodology of processing the TS data is similar as during the absolute calibration, described more in details in [16] or [25, czech only]. The recorded fast digital signal is fitted by an appropriate function and integrated in time to obtain the total intensity from all spectral channels. The shape of the TS spectrum parametrized by the electron temperature, see equation (2.11), can be determined from the ratio of signals on respective channels. The total intensity acquired by

[1] ADC = analog-to-digital converter

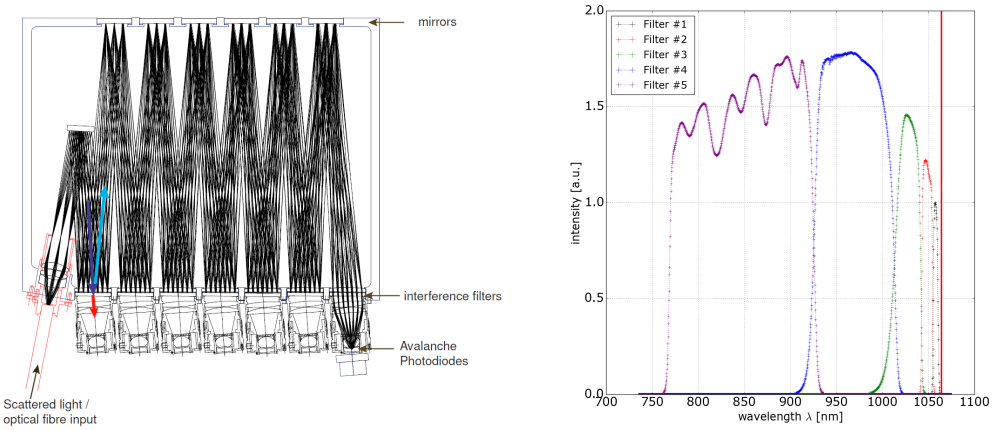

(a) **(b)**

Fig. 3.5: (a) The scheme of the filter polychromator used on the MAST and COMPASS tokamak [15], (b) the spectral transmissivity of five interference filters for polychromator #523 on COMPASS [25].

all spectral channels is proportional to the electron density, see equation (4.2), if the proper absolute calibration, which quantifies the global transmissivity factor represented as system constants, is provided.

Part II

Results

Chapter 4

Thomson scattering data processing and results

This chapter includes the description of procedures performed or implemented within the framework of this diploma thesis. The author's aim is to show the methods as a process from its motivation to the implementation with proper testing and commissioning procedures being carried out. Additional measurements and applications, which emerged during preparation of this work, are also presented.

4.1 Data processing system

The following section describes data processing system of Thomson scattering diagnostics on the COMPASS tokamak. The issue of signal collection, detection and data acquisition is covered in the Chapter 3. As mentioned in the Section 3.4, the main objective of data processing procedures is to reconstruct the spectrum of the scattered light.

As stated in the Section 3.3, the scattered light originating from the plasma region is collected by two separate sets of collection optics of the edge and core TS and transmitted by optical fibres to detectors. The TS system on COMPASS is using the duplexing technique, which enables a detection of signal from two separate spatial points within the tokamak vessel by a single detection unit (polychromator). Detectors operation is more precisely described in [20, 25, 15], and for the purposes of this work the key aspect is that transmitted signal is detected by five spectral filters or channels, which are designed for detection of the useful spectral range (750 to 1064 nm). Currently, the data from only four spectral channels are digitised and recorded, due to the limited number of available digitisers. Demonstration of typical raw data acquired during tokamak discharge number 13007 is presented in Fig. 4.1. In the figure, the fast component of the temporal evolution of the voltage U_{APD} on APD (slow component filtered by the high-pass filter in the amplifier) is displayed for all four spectral channels of four different polychromators, 504, 510, 520 and 528. Spectral channels numbering is consistent with the one presented in Fig. 3.5b, while the polychromators are enumerated using numbers from 500 to 529. The scheme on the right hand side of the same figure shows the position on the z-axis inside the tokamak vessel along the laser beam path (vertical coordinate) observed by

given fibre bundle matched to corresponding polychromator. Therefore, the position $z = 0.0$ m refers to the horizontal tokamak axis, called *mid-plane*. It is noted, that the area from which each polychromator detects signal has a shape of a rectangle due to rectangular arrangement of fibre bundles [24] and is only represented by its middle point in the figure.

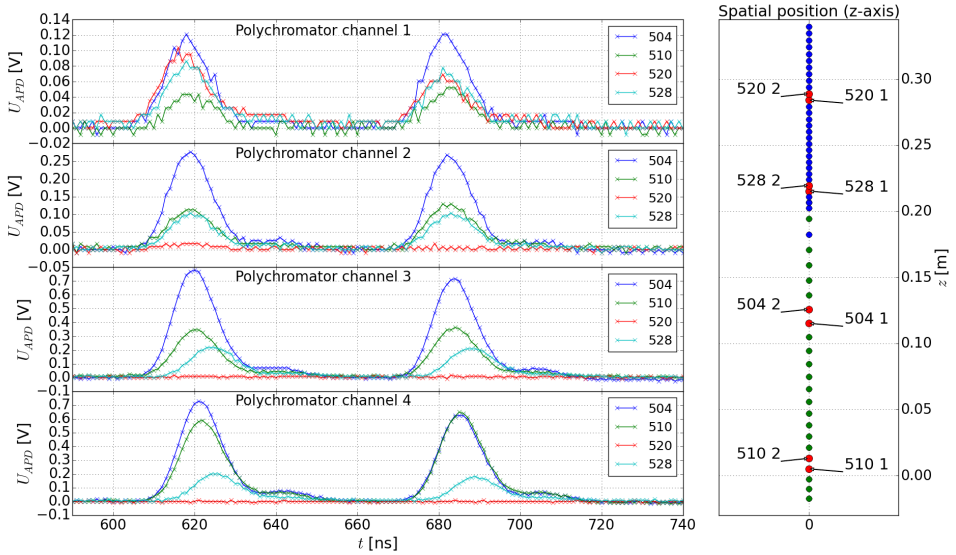

Fig. 4.1: The raw data acquired by the TS diagnostic system. The data from four spectral channels is shown for polychromators 504, 510, 520 and 528 for the tokamak discharge number 13007 for the same laser pulse inducing Thomson scattering signal during the flat-top phase of the discharge, when the plasma current remains constant.

Compared to Fig. 3.2, the core and edge TS diagnostic system are easily distinguished in the figure, blue dots represent the edge while green ones the core TS system. The number written after the polychromator specification (for example 510) specifies whether this position refers to the first (1) or to the second (2) peak shown in the left part of the same figure. Different time of arrival to the detector of the two pulses is a result of the duplexing technique, mentioned in the section 3.2. The signal from two adjacent spatial points travels through an optical fibre bundle of a different length (13 m difference) towards the detector, thus causing the time delay of approximately 66 ns. The refractive index of the optical fibre is taken into consideration. To verify this, it can be seen that the first peak, for instance in the third polychromator channel, has a maximum at approximately 620 ns and the second highest peak is located at roughly 685 ns.

The intensity of the signal is proportional to the determined electron density. In general, the higher the plasma density, the higher the intensity of the signal. Temperature determination is more complicated and is more precisely described below. From Fig. 4.1 one can see the variability of signal intensities between channels as well as polychromators. For instance, in the plasma core region both higher temperature and density is expected, that corresponds to stronger signal on polychromators 510 and 504, which observe this region. On the contrary, the polychromator 520 observing the plasma edge registers a not negligible signal only

in the first channel. This indicates low temperature and density. This is evident from Fig. 2.3, since for lower electron temperature the spectrum of the scattered light has narrower profile with the peak wavelength closer to the probing laser.

The time of arrival of the individual pulses of scattered light on APDs within one polychromator is gradually shifted forward in time, as the light has to travel additional distance of approximately 30 cm from one interference filter to another, which is evident from Fig. 3.5a.

It is observed, that each detected TS signal peak is followed by a secondary peak with variable but ordinarily lower intensity, approximately one tenth of the first peak in the terms of amplitude. The origin of the second peak reside in the requirements on the custom-made photodiodes. APDs were specified so that the voltage on them should never decrease below zero value, therefore, the secondary peak is caused by the swing on electrical circuit. In some cases, this second peak is caused by insufficient mitigation of stray light, which is discussed below.

4.2 Data processing algorithm

Up to the present day, the data processing unit is based on routines received from the Thomson scattering team on the MAST tokamak, when the COMPASS diagnostic was put into operation. The processing system, provided in IDL programming language, was adjusted to fit hardware components and arrangement of the COMPASS diagnostics and operation. Presented approach in the data processing development aims to this system review and design followed by the implementation of the new set of routines written in open-source programming language Python.

Overall flow chart representing the TS data acquisition and processing together with indispensable calibrations, which must be included in the process, is shown in 4.2. Box on left hand side is devoted to issues connected with calibrations, while the right upper part labelled **Hardware** represents data acquisition part, where a triggering unit is indicated. Right hand side box marked as **Processing** mostly describes data processing itself, where the spatial calibration section is included for the purpose of maintaining the methodology consistent. Each part of the process is described separately below and afterwards their overall combination resulting in plasma parameters determination.

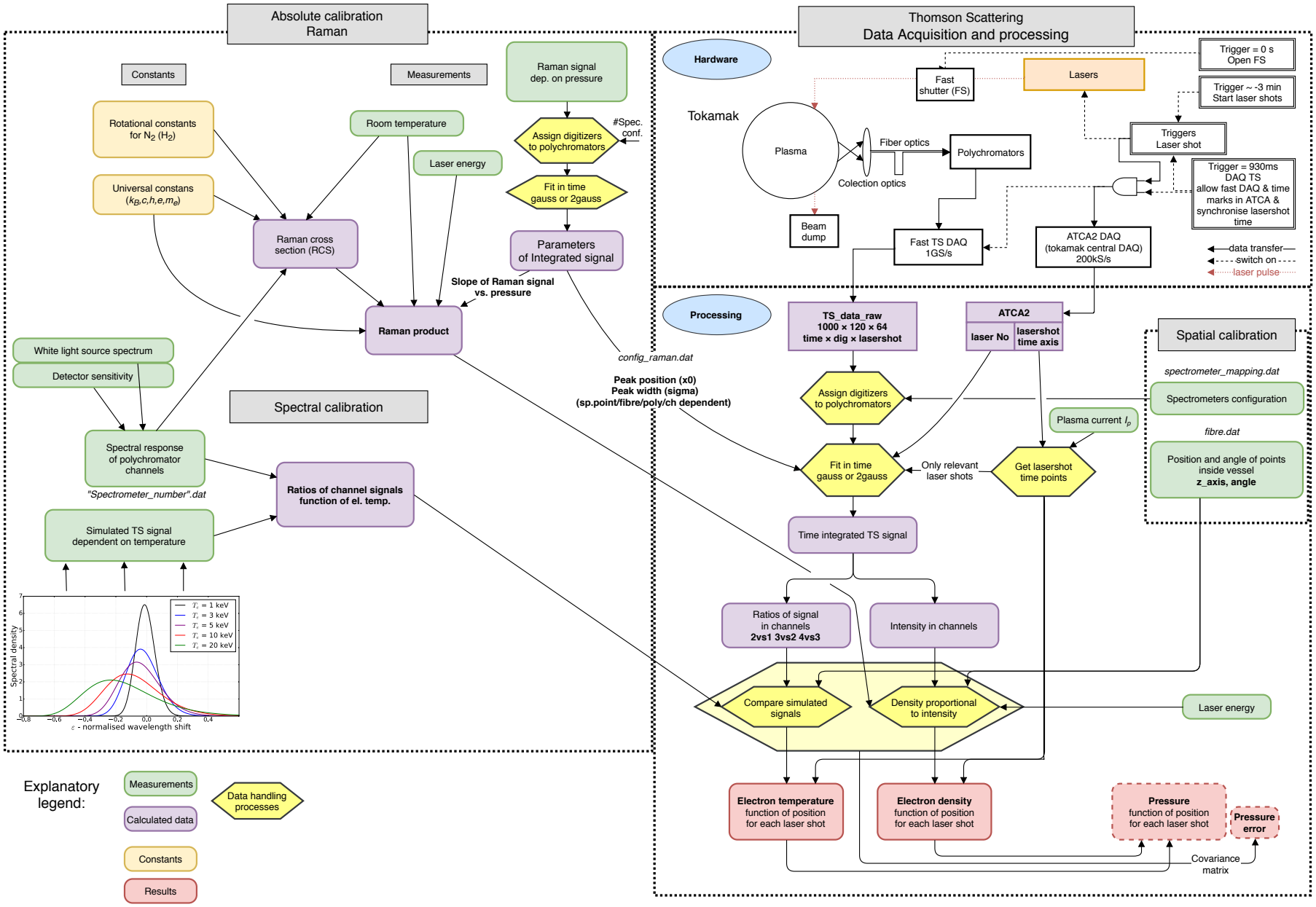

Fig. 4.2: The diagram showing data processing system for TS diagnostics on the COMPASS tokamak, further description in text.

4.2.1 Hardware part

The data acquisition part of the process is extensively described in [20, 16], therefore in this study it is covered briefly, but with strong emphasis on a triggering system. The triggering system of the COMPASS tokamak is responsible for the precise synchronisation of all included subsystems necessary for the tokamak discharge and for its successful course, thus starting indispensable systems (power sources, plasma controlling systems, etc.) together with full synchronisation of diagnostic apparatus and data acquisition.

The part of the triggering system dedicated to TS provides several functions [20]:

- laser operation
- synchronisation of lasers with each other - delay between pulses
- synchronisation to tokamak timing
- synchronisation of ADCs - for each laser
- operation of data acquisition system during the tokamak discharge

Each laser has two trigger inputs, one for flash lamps, which serves as a pumping for a laser crystal, and one for operating Q-switching, both in 30 Hz regime. After turning on the laser, achieving the thermal equilibrium of laser optics and crystal is important in order to ensure reaching optimal parameters, i.e. energy, beam profile and divergence, before the plasma discharge initialization. Therefore, a preparation sequence for flash lamps is initiated by a trigger arriving at -3 minutes before the zero tokamak time, ensuring the lasers are at full power before the plasma discharge. In the tokamak time 0 s fast shutter (FS) for laser beam is opened using another trigger signal. Usually, the tokamak discharge sequence is designed so that plasma is created at approximately t = 960 ms. The data acquisition (in graph DAQ TS) must be synchronised with laser pulses, more precisely, with the time of arrival of the respective laser pulse into the tokamak vessel. This is achieved by a trigger at 930 ms. Since this moment, triggers are both triggering laser firing pulses to the tokamak vessel and copied to the tokamak data acquisition storage unit called ATCA2 DAQ, where the signals are digitised with 200kS/s sampling frequency. Moreover, for the purposes of synchronisation the same triggers are transmitted to fast TS data acquisition units, where the acquisition process is initialised this way. Laser beams are simultaneously with the triggers travelling along their path towards the vessel and through the plasma, thus causing the generation of the Thomson scattering signal, which is collected and detected by the polychromators. Using fast ADCs the signal is digitised with 1GB/s sampling frequency.

Direct output of the DAQ system entering the processing part composes of two datasets, one containing Thomson scattering raw signals with specified dimensions, for instance (1000×120×64) at the time of preparation this thesis, that correspond to time series in nanoseconds (ns), a number of digitisers and a number of laser shot measurements, respectively. The dataset dimensions vary according to the settings of the acquisition period of the ADC and the number of used lasers. The second dataset contains time marks of each laser shot arrival to the tokamak vessel. These two datasets are the main inputs to the processing part.

4.3 The process of calibration

Additional data necessary to perform the calculation are results of various calibration routines.

4.3.1 Spectral calibration

Spectral calibration, described more in detail in [16, 25], serves as a tool for quantification of the spectral sensitivity of used spectral filters by means of introducing the source of a tunable monochromatic light to each polychromator. Relevant range of the light spectrum is scanned with a defined wavelength step, while the signal from the APDs of each polychromator channel is recorded. Using this technique the spectral transmissivity of each filter of each polychromator is evaluated. Corrections to the spectrum of the white light source and its detector sensitivity must be taken into consideration. Resulting datasets are stored in calibration files *"Spectrometer_number".dat* (for instance *523.dat*) for each polychromator. Typical results of this calibration routine for one of the polychromators are presented in Fig. 4.3a overlapped with the Thomson scattering spectrum. The increasing Doppler broadening of the spectrum with rising temperature is clearly observed, while the characteristic blue-shift of the peak position is more apparent from Fig. 2.3.

To quantify the transmission properties of the polychromator, the relative intensity acquired by each channel dependent of the electron temperature is calculated, by integrating the overlapped spectrum over the spectral dependence of filter's transmissivity, which is presented in Fig. 4.3b(left). The values of intensity for one temperature of 200 eV are highlighted. As can be seen from the same figure, when the temperature is low only the first channels are able to detect the signal, but with rising temperature the acquisition becomes distributed over all channels. For instance fourth channel starts to transmit non negligible signal once the temperature exceeds 100 eV, while the relative intensity on the first channel is dropping rapidly. Ratios of expected signals in adjacent spectral channels as a function of the electron temperature, presented in Fig. 4.3b(right), are the key quantities for the electron temperature determination, since they are dependent only on the spectrum of the scattered radiation, which is given by electron temperature. The ratios for given temperature of 200 eV are highlighted as well in the figure. In principle, determination of the electron temperature from measured signal in all spectral channels consists in finding the ratios nearest to the measured ones, which correspond to a single electron temperature value.

Spectral calibration files were provided during the commissioning phase of the construction of the TS diagnostics on COMPASS [26][czech only] and revised later in [25][czech only].

4.3.2 Spatial calibration

Spatial calibration is another part of the calibration process essential in order to achieve reliable measurements by any optical diagnostic system, including Thomson

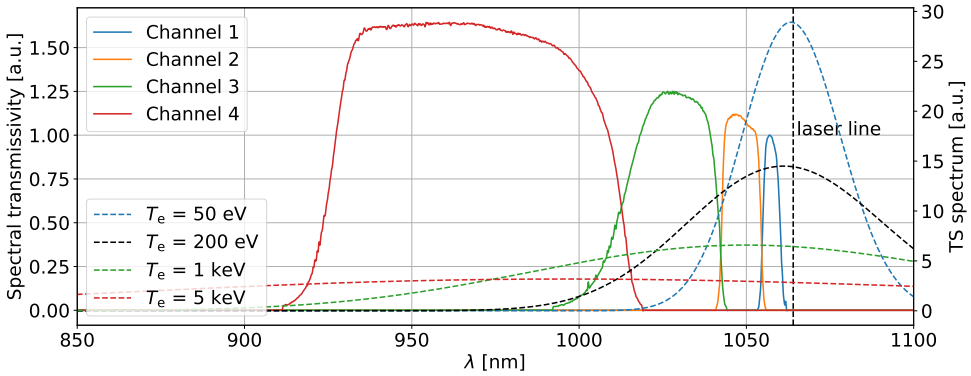

(a) The spectral transmissivity of four channels of one polychromator normed to the maximum of the first channel, overlapped with the Thomson scattering spectrum calculated for various electron temperatures. Vertical dashed line represents the laser beam wavelength.

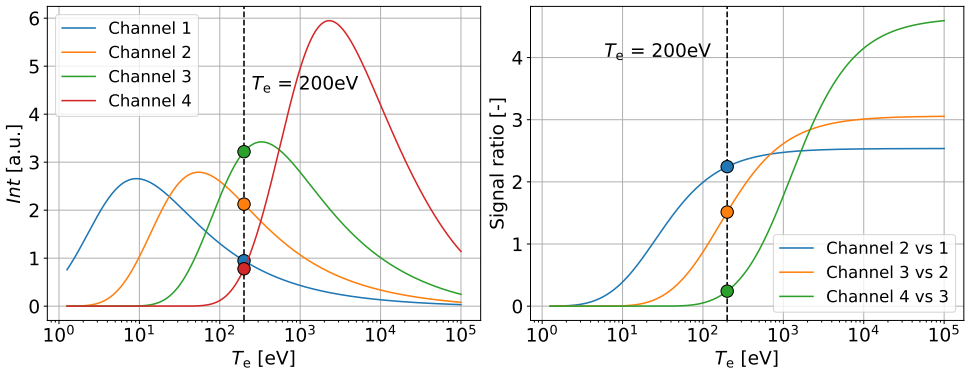

(b) Expected signals depending on electron temperature T_e on all four polychromator channels (left), ratios of the calculated signals (right). Both for polychromator number 523. Ratio values for given electron temperature of 200eV, are marked.

Fig. 4.3: Spectral calibration. Polychromator respond to the Thomson scattering spectrum dependent on electron temperature.

scattering diagnostics. In the flow chart describing the data processing Fig. 4.2, it is shown in the right middle section of the diagram. Spatial calibration of TS diagnostic system on the COMPASS tokamak is a very complex process of various routines and methods ensuring that reliable performance is achieved. Extensive effort was given to provide proper description of this part of calibration process in [20, 15, 25].

In principle, the outcome of spatial calibration consists in providing a file *fibre.dat*, which contains information about polychromators and digitisers settings together with position of each observed spatial point inside the tokamak vessel with reference to the optical system, namely their **z_axis** and scattering **angle** between the laser beam axis and line of sight. In the same section, the *spectrometers configuration* is given as one of the inputs. This part is not exactly an outcome from the spatial calibration, but rather the hardware setting of the polychromators and data acquisition units, which is used for proper assignment of ADC digitizers to the polychromator channels. Incorrect interconnection would result in wrong assignment of determined plasma parameters to the spatial points.

Additional methods and routines are performed in order to attain high precision of the spatial calibration, which is demanded as the TS diagnostics is extremely sensitive to any misalignment between the laser beam position with relation to the collection optics. If the whole cross-section of the beam, which induces the scattering in the plasma, is not imaged onto the detector input, the collected light intensity drop is interpreted as a decrease of the electron density, in the worst case the measurement is impossible. Apart from manual and visual control of the alignment by the supervising personnel of the diagnostic on a regular basis, additional tools are implemented on the majority of TS diagnostics around the world. A commonly used alignment-checking method, implemented for instance on tokamaks MAST [27], NSTX [28] or COMPASS [29], is observation of the collected light from different segments in the focus plane of the collection optics. The transmission of scattered light from the tokamak region to the detection unit is mostly done by means of fibre optics using fibre bundles composed of many individual fibres. The general idea is that signal from a segment of fibres or even from a single fibre is acquired and detected separately. From the ratio or relative portion of detected signal in different positions in the fibre bundle plane, the relative position of the laser beam and collection optics, in other words the alignment, can be assumed.

One of the points in this thesis assignment, suggests performing additional or innovative methods of calibration. Recent effort was expended on the simulation and optimization of the so-called "split-fibre" method for spatial calibration of the Thomson scattering diagnostic on the COMPASS tokamak. Application of obtained findings and results can be used to exploit the split-fibre technique to supply additional information about the diagnostic alignment, thus enhancing the method utilization. In addition, measurements of the vibrations of the collection optics can be compared with the results from the newly enhanced split-fibre method. Since both the optimization of the split-fibre technique and the vibration measurements were performed and analysed by the author of this thesis and the topic is closely related to the thesis theme, the chapter 5 is dedicated to both tasks.

4.3.3 Absolute calibration

The absolute calibration of a diagnostic system is a routine which enables the quantitative determination of exact physical values, given for a specified system. Considering Thomson scattering diagnostic, the absolute calibration is indispensable in order to determine the electron density in the observed plasma region, which is proportional to the acquired intensity of Thomson scattering signal. To provide absolute values of the density the constant of proportionality has to be determined. Following section describes the process of absolute calibration by means of the Raman scattering.

Thomson scattering signal

The total Thomson scattering signal is given by the number of measured photoelectrons n_s, which can be calculated according to (4.1), in the spectral channel and detector efficiency [15].

$$n_s = n_e\, n_{laser}\, \frac{d\sigma_{TS}}{d\Omega}\, \Delta\Omega\, T(\lambda_L)\, L\, QE \int \frac{\phi(\lambda)}{\phi(\lambda_L)} \frac{S(\lambda; T_e, \theta, \lambda_L)}{\lambda_L} d\lambda \qquad (4.1)$$

In the equation (4.1), following quantities can be distinguished, n_e and T_e represents electron density and temperature, n_{laser} is the number of photons with λ_L wavelength, previously referred to as λ_i as incident, delivered to the scattering region by a laser. Thomson scattered signal originates along the scattering length L and is observed from the solid angle $\Delta\Omega$. The differential cross-section $d\sigma_{TS}/d\Omega$ of Thomson scattering is defined in (2.7). The system transmission at the laser wavelength is given by $T(\lambda_L)$, while the spectral transmission of the optical filters $\phi(\lambda)$ is normalised to the spectral transmission at the wavelength. Spectral function S corresponds to the one previously derived, see (2.11). QE represents the quantum efficiency of the APD[1].

Thomson scattering signal, V_{TS}, is then given by the number of photoelectrons multiplied by the APD gain factor. The terms in latter equation can be distinguished into, known constants, system constants, results from spectral calibrations (spec. cal.) and quantities measured for each scattering event (meas.), which are scattered signal V_{TS} and laser energy E_{laser} [15]. Number of photons in the laser beam n_{laser} can be calculated as laser energy divided by energy of a single photon hc/λ, where h represents the Planck constant. Parameters n_e and T_e highlighted in bold, which is included implicitly as a parameter of the spectrum of the scattered light, are determined from this term if all the other quantities are known.

$$\underbrace{V_{TS}}_{\text{meas.}} = \underbrace{(G\Delta\Omega\, T(\lambda_L)\, L\, QE)}_{\text{system constants}} \underbrace{\left(\frac{1}{hc/\lambda_L} \frac{d\sigma_{TS}}{d\Omega}\right)}_{\text{known constants}} \mathbf{n_e}\, \underbrace{E_{laser}}_{\text{meas.}} \int \underbrace{\frac{\phi(\lambda)}{\phi(\lambda_L)}}_{\text{spec. cal.}} \frac{S(\lambda; \mathbf{T_e}, \theta, \lambda_L)}{\lambda_L} d\lambda \qquad (4.2)$$

In order to determine electron density from the measured V_{TS} the system constants from previous equation must be evaluated by means of an absolute calibration. In the following section the basics of the Rayleigh and Raman scattering are briefly introduced, as they are a commonly used tool for the absolute calibration. The Thomson scattering diagnostics on the COMPASS tokamak is absolutely calibrated by means of the Raman scattering process, therefore, is described more in detail.

Raman scattering signal

The total signal measured V_{Ram} by the same equipment as for the COMPASS TS is the integral in time of the Raman scattered pulse and can be written as follows similarly to (4.2)

$$V_{Ram} = n_{gas}\, n_{laser}\, \frac{d\sigma_{Ram}}{d\Omega}\, \Delta\Omega\, T(\lambda_L)\, L\, QE \int \frac{\phi(\lambda)}{\phi(\lambda_L)} \frac{S_{Ram}(\lambda)}{\lambda_L} d\lambda, \qquad (4.3)$$

[1] APD = avalanche photodiode, device commonly used for detection of Thomson scattering signal.

for a medium gas density of n_{gas}, differential cross-section of Raman scattering process $\mathrm{d}\sigma_{\mathrm{Ram}}/\mathrm{d}\Omega$ and its spectral distribution $S_{\mathrm{Ram}}(\lambda)$, remaining quantities are defined above . One can regroup the terms in the latter equation into system and known constants, variables and measured quantities. Moreover, discrete values of Raman scattering signal reduce the integral into summation over shifted wavelengths λ_J. [15]

$$\underbrace{\frac{V_{\mathrm{Ram}}}{P_{\mathrm{gas}}}}_{\text{variables}} = \underbrace{(G\Delta\Omega\, T(\lambda_{\mathrm{L}})\, L\, QE)}_{\text{system constants}} \underbrace{\left(\frac{1}{hc/\lambda_{\mathrm{L}}} \frac{\mathrm{d}\sigma_{\mathrm{Ram}}}{\mathrm{d}\Omega} \frac{1}{k_{\mathrm{B}}} \sum_J \frac{\phi(\lambda_J)}{\phi(\lambda_{\mathrm{L}})} S_{\mathrm{Ram}}(\lambda_J) \right)}_{\text{known constants } (\phi \text{ from spec. calib.})} \underbrace{\frac{E_{\mathrm{laser}}}{T_{\mathrm{gas}}}}_{\text{measured}} \tag{4.4}$$

In both equations (4.2) and (4.4), identical set of system constants can be identified. The general objective of the absolute calibration is quantification of this global factor, which determines the efficiency of light detection and subsequent signal acquisition of the whole system enabling determination of the electron density n_{e}, which is proportional to the signal intensity.

While the whole portion of Rayleigh scattered light is polarized parallel to the polarization of the incident wave, Raman scattering light has two polarizations, both parallel and perpendicular to the incident wave one, see (4.5), where $\eta_\perp$ and $\eta_\parallel$ signifies the relative efficiency of the TS system in the polarizations perpendicular and parallel to the incident light. The Thomson scattering light is polarized parallel to the polarization of the incident wave, therefore, a polariser is a commonly used element to reduce the background and stray light signal during the standard operation of the diagnostics, as it is in the COMPASS TS. In such case, only parallel polarization of Raman scattered light must be considered, i.e. $\eta_\perp = 0$. [15]

$$\sigma_{\mathrm{Ram}} \rightarrow \left(\eta_\perp \frac{3}{7} + \eta_\parallel \frac{4}{7} \right) \sigma_{\mathrm{Ram}} \tag{4.5}$$

Absolute calibration routine

Absolute calibration of the TS system on the COMPASS tokamak is performed by means of rotational Raman scattering in nitrogen gas (N_2), whose theoretical principles are covered in section 2.3. As stated in the section, since the laser wavelength is 1064 nm and the polychromators transmits only signal shifted towards lower wavelength, only anti-Stokes lines for N_2 are considered. Absolute calibration of the diagnostic system supposed to be provided on a regular basis to control current situation. The calibration process could be divided in two stages. Firstly, the quantity referred to as *Raman cross section (RCS)* is computed for each polychromator according to (2.14) as a product of Raman lines and spectral transmissivity of proper polychromator channel, which is integrated over the Raman scattering spectrum. Nitrogen anti-Stokes Raman lines are presented in the top graph in Fig. 4.4 together with the first two spectral filters of a given polychromator. Transmissivity of spectral channels is normalized to the maximum of the first channel. Shown intensities are calculated according to (2.20) using the rotational constants for the nitrogen gas

molecule, presented in Tab. 2.3 and universal physics constants. The bottom part of Fig. 4.4 shows the portion of Raman signal in the given spectral channel of the same polychromator. Values in the legend represents the aggregate value, i.e. the Raman cross section, for corresponding spectral channel. The identical calculation is performed for all polychromators and results for the first two spectral channels are displayed in Fig. 4.5.

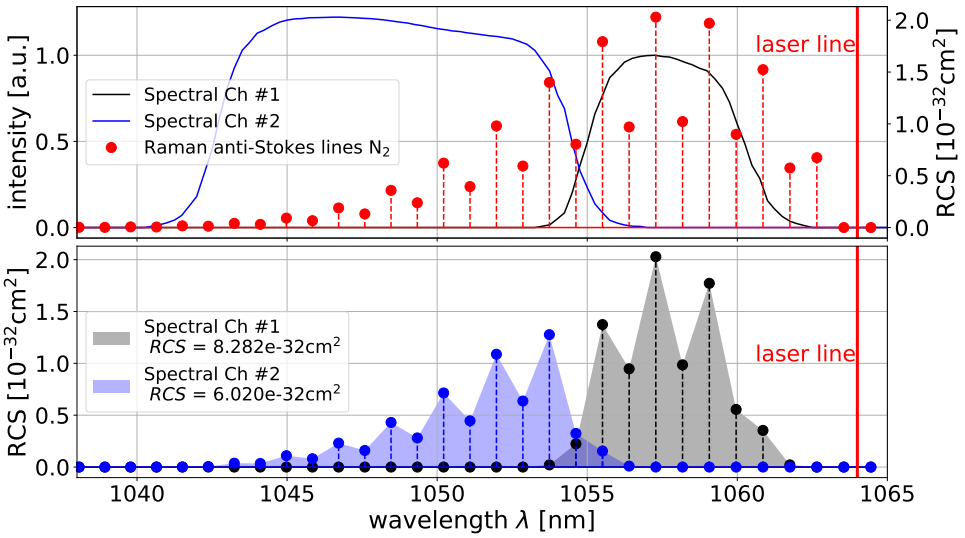

Fig. 4.4: Scheme for Raman cross section (RCS) calculation. In the top part intensities of anti-Stokes Raman scattering lines in N_2 are presented overlapped with spectral transmissivity of the first two channels of a given polychromator normalized to the maximum of the first channel. The bottom part shows the portion of the scattered light belonging to corresponding spectral channel, where only discrete values are considered. Filling colour is displayed only a highlighting purpose. Value *RCS* in the legend represents the Raman cross section for given spectral channel. Laser wavelength is signified by red line on the right, $\lambda_L = 1064$ nm.

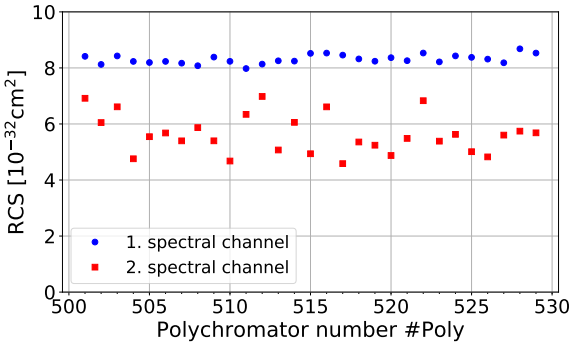

Fig. 4.5: Computed RCS for the first two spectral channels of all polychromators.

For the second stage, i.e. the computation of so-called *Raman product*, performing experimental measurement of the Raman scattering is required. Tokamak vessel is filled with proper gas, nitrogen on the COMPASS tokamak, at measured room temperature T_R. The detected signal of Raman scattering induced by the laser pulse

of energy E_l is recorded. Measurement is done for each laser individually, while the pressure of the gas P_{gas} is held constant. As can be seen from the equation (4.4), the Raman scattering signal is linearly proportional to the pressure in the scattered medium. Therefore, the slope of this proportion becomes is the key quantity for the absolute calibration and the pressure of internal gas is being gradually decreased and the measurements is repeated for chosen values of the pressure. Number of records for each pressure and each laser is set high enough to provide sufficient statistics. On the COMPASS tokamak 60 measurements for each pressure are recorded. Averaging over valid records is included in the post processing process. The laser energy E_l is supposed to be monitored and recorded routinely. The Raman product $R(i)$ for polychromator i is afterwards computed using equation

$$R(i) = T_{gas} k_B \frac{r_e^2}{RCS(i)} \frac{k(i)}{E_{laser}}, \tag{4.6}$$

where k_B and r_e refers to Boltzmann constant and classical electron radius, respectively. The formula for the Raman factor can be derived if the equations (4.4) and (4.2) are compared. The quantity r_e^2 originates from the differential cross section of the Thomson scattering in (2.7). According to the theory, integrated signal of Raman scattering suppose to have a linear dependence on gas pressure and $k(i)$ signifies the slope of its linear fit. To assign detected signal from digitisers to the proper polychromator the *spectrometer_mapping.dat* file is used (signified by @Spec.conf. in Fig. 4.2). The process of fitting and integrating the acquired raw Raman signal from each individual laser shot in the fast data acquisition units is the same as for the standard Thomson scattering signals and, therefore, is described in the section (4.4) devoted to the proposed data processing routine for TS. The typical integrated signal acquired by the first two spectral channels of polychromator 506 is shown in Fig. 4.6a together with linear fit. Relative errors of the shown fits are less then 0.5%, which is negligible in comparison to other error sources. The issue of errors is discussed afterwards.

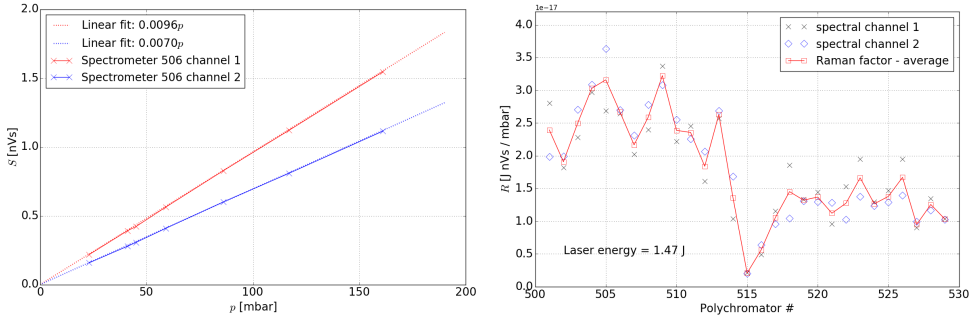

(a) **(b)**

Fig. 4.6: (a) Integrated Raman signal dependent on gas pressure for the first two spectral channels for polychromator 506. (b) Raman factor computed for all polychromators for laser 1 and pulse 1 (see 4.1). Signal from 1. and 2. spectral channels is averaged.

This method of absolute calibration on the COMPASS tokamak must be performed under strict requirements. First of all, in order not to contaminate cleanness of the

tokamak vessel, where high vacuum ($<10^{-5}$Pa) is maintained, a high purity nitrogen (N_2) is used. The value of gas pressure is limited due to possible breakdowns in the gas when the value is too high. Experimentally was discovered that the pressure is supposed to be kept under 200 mbar. Additionally, while the nitrogen is being filled into the vacuum vessel, a dust seated on the bottom becomes whirled and might cause not negligible amount of breakdowns in gas. Breakdowns represent significant sources of broad-spectrum stray light with different non-Gaussian shape, which is introducing a undesirable signal and might alter the result of absolute calibration if not detected during the post processing. Recently, it was found, that the dust is most likely candidate for the source of breakdowns. The last absolute calibration by means of the Raman scattering was carried out two days after the nitrogen was filled into the vacuum vessel. Such a delay was proven to be long enough for the whirled dust to be settled and the breakdown occurrence was nearly mitigated. The frequency of randomly appeared breakdowns is increasing with the gas pressure. Nevertheless, the scenario when enough time is given to the dust particles to settle and the upper gas pressure limit is established at 200 mbar is proposed as a preferred scenario for performing future absolute calibration routines.

One of the points in the assignment of this thesis comprises in incorporation of results of calibrations into the data processing algorithm. Previously presented calibration routines, which are indispensable for proper operation of the TS diagnostics on COMPASS and are included in the data acquisition and processing diagram in Fig. 4.2, are successfully incorporated into the data processing algorithm in Python by the author of this thesis. The absolute calibration routine as described above, is implemented completely, from the theoretical calculation of the anti-Stokes Raman lines to the processing of measured raw data, in order to provide consistent and unified set of routines in one programming language, Python, to avoid unnecessary

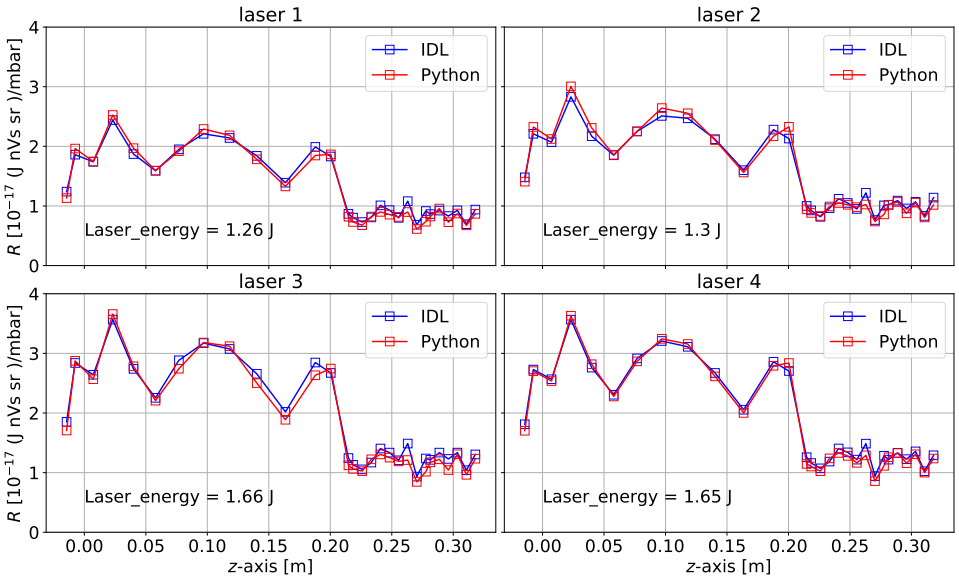

Fig. 4.7: Calculated Raman factor R as the key result of the absolute calibration process. Laser energy is indicate for each laser individually.

interconnection with IDL programming language. Comparison of calculated Raman factor R according to (4.6) using the newly developed and implemented routines in Python by the author of this thesis and the routines implemented in IDL language is presented in Fig. 4.7. Measurements were done during the latest absolute calibration in March 2018. Despite the fact, that the results are in good agreement, more detailed commissioning phase to verify the results and compare the correctness of both sets of routines is planned to be performed.

During the implementation of the absolute calibration routine, several software optimization processes and precautions emerged to enhance the reliability of this calibration technique. Additionally, the detailed analysis of the measured data, which also contributed to better understanding of the data and their interpretation. The techniques, developed and implemented by the author of this work, which made a relevant contribution considering the absolute calibration, are presented below.

Optimization o absolute calibration

Firstly, the mentioned problem of Raman scattering signal altered by undesirable phenomena, for instance, by the electrical breakdowns occurred in the gas, when the laser travels through the tokamak vessel.

Three methods of such bad records recognition are proposed by the author to be implemented to the standard Raman scattering evaluation. First is based on checking saturated records. The sensitivity of each detector and its gain settings state the saturation value for which collected data can be checked. The saturation implying the loss of useful signal of the substantial part of the signal peak leads to incorrect determination of fitting parameters. Therefore, the first routine is based on detecting the saturated channels. Second routine observes the time evolution of collected light and checks its Gaussian shape. Moreover, due to the character of Raman scattering (see Fig. 4.4) only first two spectral channels of a polychromator are assumed to acquire useful data, therefore detecting signal in third and fourth channel suggests its different nature and these records are excluded. Also records with insufficient intensity of the scattered light, that rarely occur especially when the nitrogen pressure is low, are not used for calculation. Automatic detection of bad records is currently being tested and its optimisation on newly performed Raman scattering measurement is indispensable for its commissioning.

Absolute calibration is resulting in computation of Raman product $R(i)$ for whole set of polychromators, see equation (4.6). Result of most recent calculation for one laser is shown in 4.6b for both first and second spectral channels of each polychromator. The red line signifies the the average value, i.e. the resulting Raman product for each polychromator is taken as an average value. Energy of corresponding laser is given. It can be observed that the Raman product varies significantly with the polychromator number. Polychromators 515 to 529 belong to the edge TS therefore lower values of Raman product are expected, as seen in the figure, mainly due to the linear dependence on scattering length, which defines the spatial resolution of the diagnostics. Edge TS on the COMPASS tokamak has 3 mm resolution, while in the core region it extends to 10 mm, therefore in the edge TS a signal with intensity of approximately one third of core TS is expected. Also more

complicated geometry of collection optics of edge TS might decrease the amount of detected signal.

Aim of proposed Raman scattering data processing method is to provide automated system capable of performing self-sufficient calculation of Raman cross section and Raman product for all polychromators, without the necessity of human intervention or supervision, which is nowadays almost inevitable. As mentioned before, achieving this goal still requires series of testing and optimisation process.

By-product of absolute calibration data processing is a creation of configuration file (*config_raman.dat* mentioned in the diagram Fig. 4.2), which contains averaged values of the fitting of temporal evolution of scattered signal, namely pulse peak position $\mathbf{x}_0$ on the time axis[2] and temporal width σ of both the Raman signal and the secondary peak, see Fig. 4.1. Meaning of mentioned parameters is given from a form of the Gauss function used during the fitting procedure

$$\mathbf{f}(\mathbf{x}) = \mathbf{A}\exp\left(-\frac{(\mathbf{x}-\mathbf{x}_0)^2}{2\sigma^2}\right). \tag{4.7}$$

Data from configuration file are planned to be used as initial values for the fitting routine of TS signal during operation, if the parameters show constant tendency. Recent analysis showed the evolution of the parameters $\mathbf{x}_0$ and σ in pursuance of one Raman scattering calibration. Results for polychromator 506 are given in Fig. 4.8, where one can see the evolution of the fitted Gaussian peak parameters, $\mathbf{x}_0$ and σ of the first Gaussian peak (Raman signal). Both figures resemble similar tendency, that with increasing pressure the value of parameters decreases. This feature and its cause is yet to be resolved. Also there is a significant discontinuity between pressure values around 45 mbar, which can be observed in all data sets. This effect is probably caused by changing the ADC gain which is necessary to detect signal of order of magnitude different intensity. In addition, the Fig. 4.8a shows the dependence of $\mathbf{x}_0$ on the laser number. Peak position of laser 1 varies around 616 ns while for the laser 2 around 619 ns. Laser beams are driven to the tokamak vessel by nearly the same laser path, where maximally a 30 cm difference between distances the beams travel could be noticed. The effect is therefore rather caused by a tolerance of electronic components inside laser drivers. On the other hand, the Fig. 4.8b shows the dependency of peak width (σ) on polychromator channel number. The pulse peak width is more related to the characteristics of the detector. Therefore, as each channel is provided with one detector, even though from the same production series, the components characteristics may vary in a range of percent if they fulfil tolerance limit. These phenomena supports the idea to use this values as an initial estimation for given parameters, since it shows that the values are laser or channel specific, although there is a non-negligible trend with respect to nitrogen pressure. Moreover, the parameters of fitted curve show slightly different values across the set of polychromators.

[2] $\mathbf{x}$ represents time axis in the ADC unit. This time series is by no means related to tokamak time or triggering system, therefore the $\mathbf{x}$ and $\mathbf{x}_0$ designation. From this point $\mathbf{x}_0$ is called *peak position* and σ *peak width*.

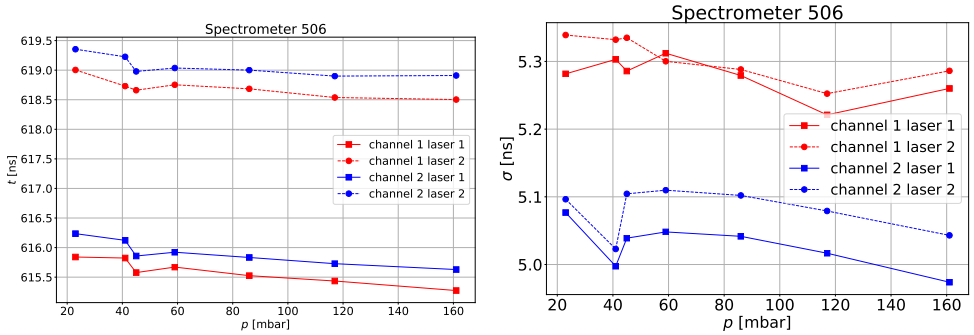

(a) **(b)**

Fig. 4.8: Results of the fitting routine for latest Raman calibration for first and second channel of polychromator 506 for both lasers: (a) position of the peak center $\mathbf{x}_0$ (b) parameter σ of the gaussian peak.

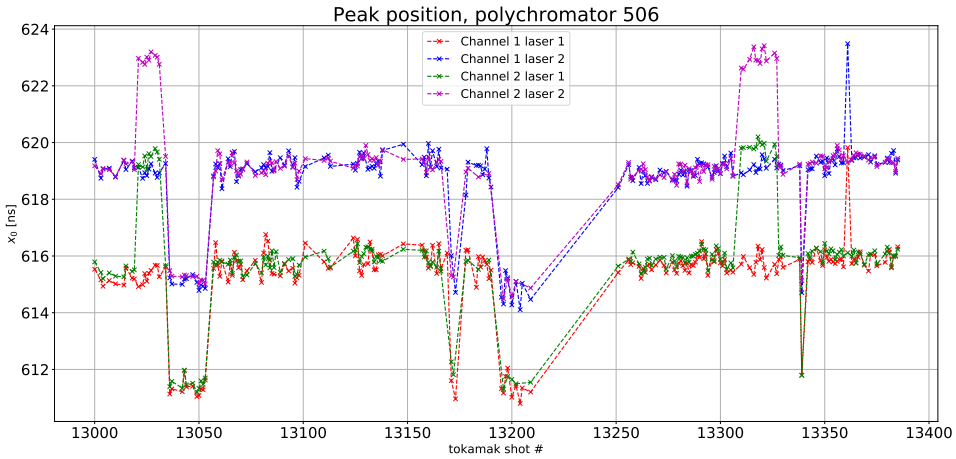

Fig. 4.9: Evolution of the fitting parameter $\mathbf{x}_0$ (signal peak position) for the first two channels of polychromator 506 for both lasers for given tokamak shot range.

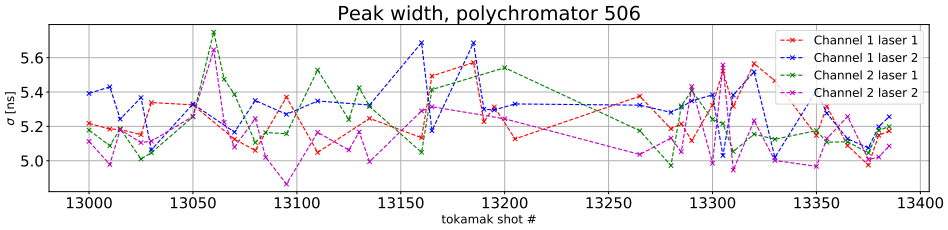

Fig. 4.10: Evolution of the fitting parameter σ (signal peak width) for the first two channels of polychromator 506 for both lasers for given tokamak shot range. Not all successful measurements are displayed, for clarity reasons.

Signal peak position analysis

Alternative approach could take into account all values previously obtained during standard fitting procedure of TS, which is described more in detail in 4.4. To perform

initial testing a simple routine was written in order to observe the evolution of fitting parameter $\mathbf{x}_0$ for chosen polychromator. Results for the first two channels of the polychromator number 506 in order to provide comparison with previous results on approximately 500 tokamak discharges for both lasers are presented in Fig. 4.9. Firstly, non-constant behaviour of the parameter is apparent. Its value varies from 610 to 625. Significant, from shot to shot, changes of the peak position are observable and would have a negative effect on initial parameter estimation, since the changes are abrupt. Nevertheless if the steps are neglected, slowly increasing trend of the peak position is observed.

If compared with the results presented in the previous section in Fig. 4.8, the values of the main trend (steps excluded) are in a good agreement. For laser 1 for both channels the value fluctuates around 616 ns and for the laser 2 around 619 ns. This outcome indicates possible beneficial usage of this method. Brief analysis shows that some of the steps are result of a change of tokamak and diagnostics operation period, for example day, week or campaign, probably when a complete restart of systems was performed. Additional analysis of the peak position behaviour with emphasis on mentioned sudden changes is necessary in order to prove this method to be useful.

To complete and expand the analysis, a comparison of signal width is useful. Its evolution, described by the parameter σ, for the same period is shown in Fig. 4.10. No similar behaviour of σ to the one shown in Fig. 4.8b is indicated by the displayed data. Values of all channels for both lasers fluctuates between 5.0 to 5.7 with no clear trend. Nevertheless, it seems that it is possible to bound the parameter σ during the fitting routine to a given range and use an average value as initial.

In general, using parameter constriction during the fitting procedure is a very useful and in this case necessary technique in order to perform stable and robust computation. The most important issue is to separate the two peaks, the first containing useful Raman or Thomson scattering data and other one caused by the mentioned electric circuit feature or possible stray light, which is done by bounding the parameter $\mathbf{x}_0$.

Similar computation was performed for the third channel of the polychromator number 507 for approximately 2000 tokamak shots, see Fig. 4.11. Resembling observation can be performed for this case. There could be distinguished several linear trends of the peak position, for instance from tokamak shot number 9100 to 10050 approximately, and then there are several noticeable steps, e.g. after 10050 or 12300. Also various short-time or point deviations from the leading trend occurred, if even consider it as a trend. Gradual degradation or slowly changing properties of electronic components inside control units could cause the drifting features. On the other hand, the issue of synchronisation various hardware clock rates is probably responsible for the sudden steps, since tokamak triggering and data acquisition of TS use their own, and are synchronised every time the systems restart is performed. It could be resolved by using one system clock rate, when it is proven to be the cause.

Furthermore, one can notice the switch between the peak positions of the lasers (blue and red dots) around tokamak shot 11300 and then back again slightly before the shot number 13000. In the concerned area, highlighted by green colour in the figure, input cables for the laser triggering were accidentally swapped with each

other. The problem was revealed and fixed afterwards with aid of this routine.

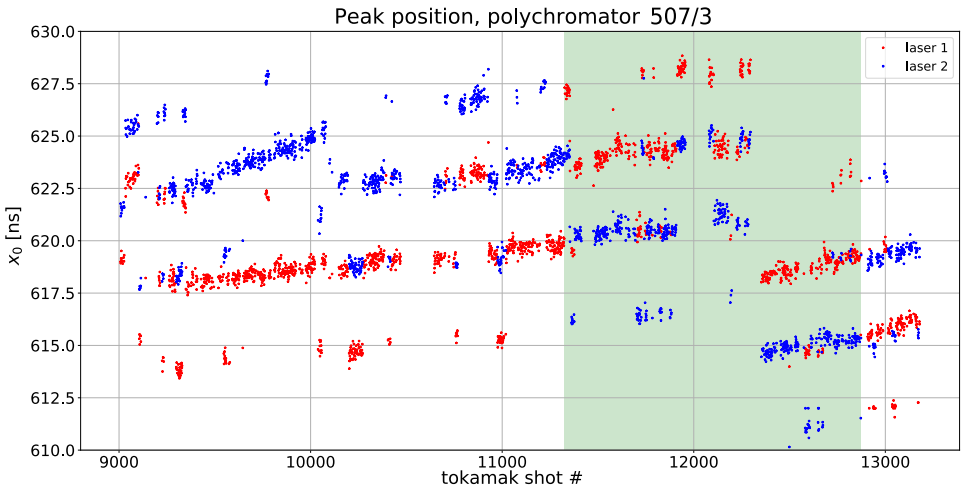

Fig. 4.11: Evolution of the fitting parameter $\mathbf{x}_0$ (signal peak position) for the third channel of polychromator 507 for both lasers with respect to tokamak shot number. Green area represents a period when cables for triggering of lasers were accidentally swapped.

4.4 Processing part of the data processing algorithm

In the following section, the procedure concerning the determination of desired plasma parameters, electron temperature T_e, density n_e and pressure p_e, from the fast raw signal recorded by ADC converters combining all previous results is considered.

4.4.1 Thomson scattering signal processing

As mentioned before in the paragraph **Hardware part**, the output of the data acquisition system consists in two data sets, **TS_data_raw**, where raw data from digitizers are stored, and time series with trigger pulses, which are identified with laser number, from ATCA2 data acquisition device. The goal of the processing routine is to recognize and sort the input data, fit relevant detected signal and integrate the results of calibration routines in order to provide electron temperature, density and pressure.

Firstly, the Thomson scattering raw data, demonstrated in Fig. 4.1, are assigned to the right polychromator, channel and spatial point, where the calibration file *spectrometer_mapping.dat* is applied. Standard regime enables 16 measurements by each laser during a tokamak discharge. Only relevant laser shots, when the plasma is present inside the vessel, are chosen to be subsequently processed. Plasma current is a stable measured quantity, that it is used to determine breakdown and duration of discharge, thus, the time range for laser shots is stated. Sorted and assigned data are then fitted in time using proper formula, by the same routine as during the absolute calibration process. At this stage, using of initial values for parameter estimation

by previously discussed method, is proposed to be integrated. Double Gaussian function $\mathbf{f}_{2G}(\mathbf{x})$, given by 4.8, is proposed as a more suitable function for detected TS and Raman signal on the COMPASS tokamak than single Gaussian, which is used currently. Applying this tool, the influence of undesirable signal or stray light is suppressed. Quantities with lower index 1 refer to the TS (Raman) signal, while the second peak (possible stray) is indexed by number 2.

$$\mathbf{f}_{2G}(\mathbf{x}) = \underbrace{\mathbf{A}_1 \exp\left(-\frac{(\mathbf{x}-\mathbf{x}_{01})^2}{2\sigma_1^2}\right)}_{\mathbf{f}_1(\mathbf{x})} + \underbrace{\mathbf{A}_2 \exp\left(-\frac{(\mathbf{x}-\mathbf{x}_{02})^2}{2\sigma_2^2}\right)}_{\mathbf{f}_2(\mathbf{x})} \tag{4.8}$$

For illustrative purposes and to clarify meaning of the parameters present in the function, an example of fitting procedure result is shown in 4.12 for one measurement of TS signal. Points (crosses), shown in the figure, represents time evolution of raw data Int_{APD} from APD acquired by digitiser, collected by given polychromator channel, for given laser shots (LS). Two peaks are able to be distinguished, the first one at the position $\mathbf{x}_{01}$ with width σ_1 and much higher intensity $\mathbf{A}_1$ represents TS signal. The second at $\mathbf{x}_{02}$ with σ_2 width and intensity $\mathbf{A}_2$ refers to collected stray light or otherwise misleading signal. For illustrations, the graph legend shows fitted values of parameters together with their standard deviation designated by Δ. Due to lower intensity of the secondary peak signal, noise and uncertainty of the fitting process has more noticeable effect, which results in larger errors. Primarily, when $\mathbf{x}_{02}$ and σ_2 are determined.

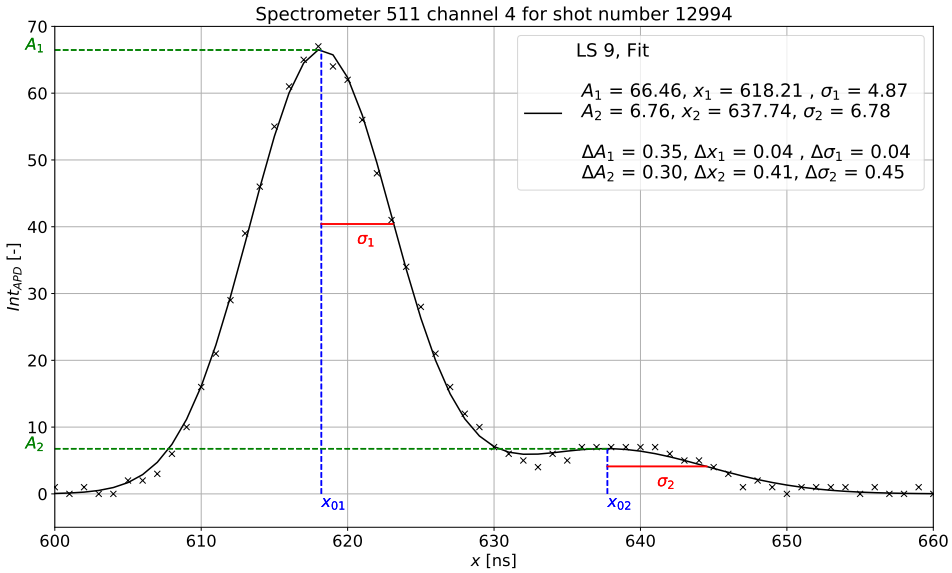

Fig. 4.12: Example result of the fitting procedure using the function 4.8, when applied on detected signal for one Thomson scattering measurement by 4^{th} channel of 511 polychromator with ninth laser pulse during tokamak shot 12994.

Additional examples of results of the fitting procedure of detected signal are shown in the figures Fig. 4.13, to provide more detailed analysis and understanding of this issue. Upper and lower parts of each graph refer to different subsequent laser

shots (LS in the legend), where laser number and the laser shot time is specified. As a result of duplexing technique, described in the section 3.2, two regions with measurable signal are supposed to be detected by one polychromator, therefore two main peaks are visible, the first around 620 ns and the second at 680 ns.

Stray light

Apart from the TS signal, each of them is followed by another peak of various intensity. It is assumed that the first peak represents useful TS data, while the second one is either cause by the feature of the APD electric circuit or it refers to the stray light signal, which is mostly visible from the figure Fig. 4.13a around 640 ns and 720 ns. In both cases the elimination of the second peak signal is favourable. In this case the secondary peak is surely caused by stray light. Such high magnitude of stray light as seen in the same figure of comparable intensity to the first peak of the signal is not a result of a flawless operation and is indicative of a laser misalignment or different mechanical obstruction, that cause undesired reflection or scattering. Standard fitting of shown signal by one Gaussian curve would result in incorrectly estimated parameters.

Proposed method of fitting the signal with double Gaussian curve is able to mitigate or reduce the impact of stray light, as seen from the figure. The dotted line in each graph represents function $\mathbf{f}_1(\mathbf{x})$ from (4.8), therefore only the TS signal. The function corresponds very well with the left half of the peak. As a consequence of the stray light in the right half it deviates to an extent given by the magnitude, width and position of the stray light signal peak. For instance, in 4.13a stray light intensity $\mathbf{A}_2$ is comparable or even larger than TS signal $\mathbf{A}_1$, while in figures (b) and (c) stray light has comparable intensity with the one in (a) but relatively to the TS signal is much lower. It reaches to approximately 15% and 6% of the TS signal in figures (b) and (c), respectively. Black solid and red dashed vertical lines represent boundaries for parameters $\mathbf{x}_{01}$ and $\mathbf{x}_{02}$, respectively. Fitting range is given specifically for each polychromator, channel and laser number, which was at this stage based on the observation of parameters of standard TS data. Difference between the two laser pulses was discussed previously and the relative shift of approximately 4 ns is considered. Design of detectors, shown in 3.1 and one polychromator more in detail in 3.5a, gives different time of flight of collected light towards one channel and APD. The distance the light travels between two filters is approximately 30 cm, therefore in takes 1 ns. As seen from figures (b) and (c), for LS 9 the first peak on the third channel $\mathbf{x}_{01}$ = 616.21 ns while for the same LS the fourth channel gives $\mathbf{x}_{01}$ = 619.24, therefore the difference is three times higher. It suggests that other factors than the time of flight have substantial impact.

Examination of the stray light peak position could help with determination of its origin and possible source. From Fig. 4.13a one can notice that the stray light is delayed by $\Delta t_{SL} \approx$ (643 - 623) ns = 20 ns. Over this time light travel the distance of approximately 6 meters. As mentioned in the section 3.1 about laser system on the COMPASS tokamak, laser beam path is terminated by a beam dump situated 2.5 meters below the horizontal axis of vacuum vessel. When both the distance towards the beam dump and back to the plasma region are considered, it correspond

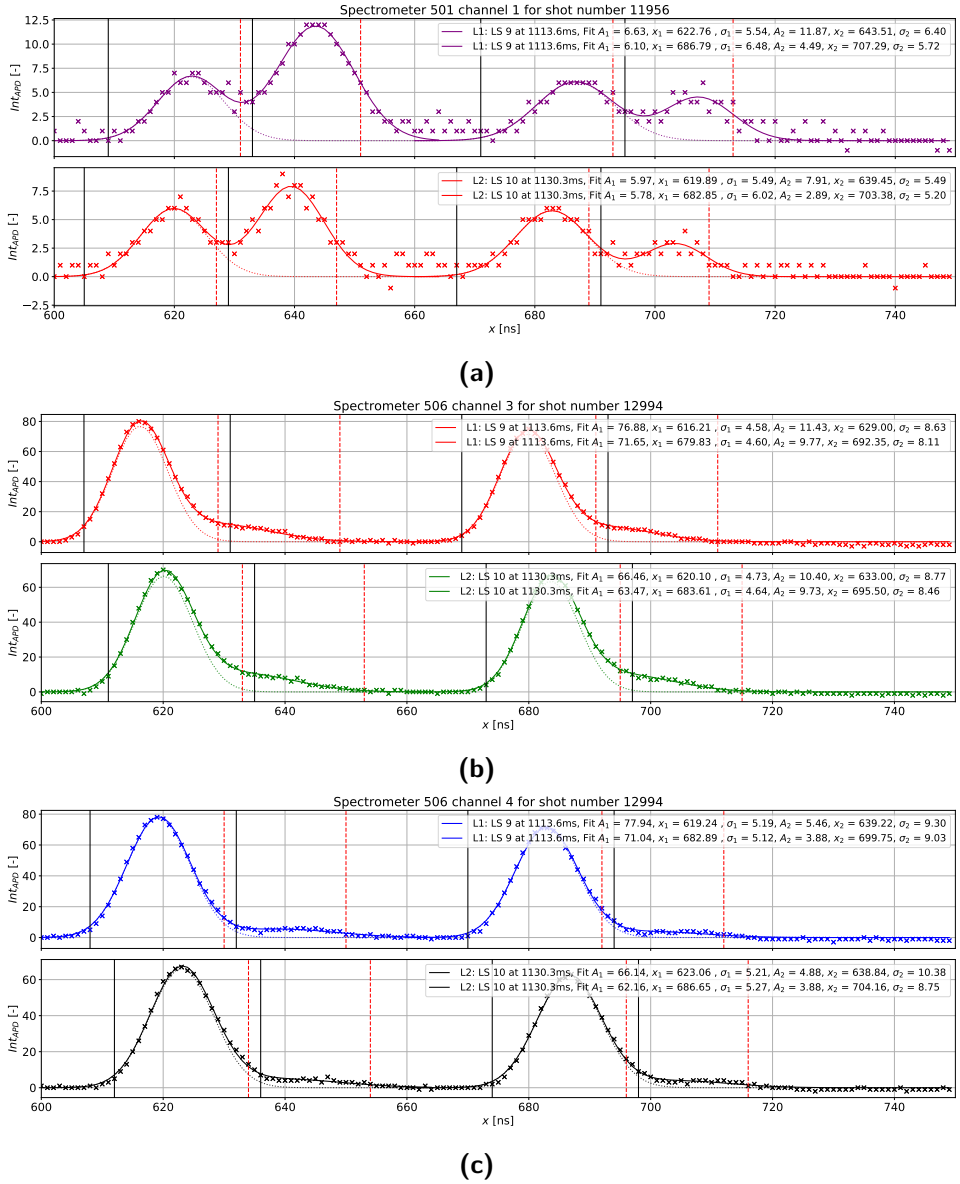

Fig. 4.13: Example of the fitting procedure of TS signal for polychromator (a) 501, channel 1 (b) 506, channel 3 (c) 506, channel 4. Both peaks, which are result of the duplexing method, are processed. Fitted parameters match their description in 4.8. Dotted line represents Gaussian shaped curve of TS signal only, i.e. $\mathbf{f}_1(\mathbf{x})$.

well with the stray light delay. Probably an unwanted reflection or dispersion of the laser light happens on the laser beam dump or when it travels through laser path. To illustrate the effect of undesirable reflection, in the Fig. 4.14 is shown the signal from one tokamak discharge, when one of the shutters in the laser beam path beneath the tokamak vessel was not open properly and partly cut off one of the laser beams, thus becoming a significant source of stray light. The figure shows detected signal from 2 laser shots of each laser by first and second channel of the of polychromator 505. Significant stray light is most observable in upper part of Fig. 4.14a and also to some

extent in Fig. 4.14b, therefore only for laser 1 (L1), which is probably caused by a difference between beam path of the lasers. Clearly, the stray signal is laser induced, because in each laser shot it arrives at the same moment after the useful signal. The fact that the highest intensity signal is acquired by the first channel, suggest that the cause of the undesirable signal is the stray light, as its wavelength is close to the wavelength range of the first spectral filter. When the obstruction was removed stray light of this intensity disappeared.

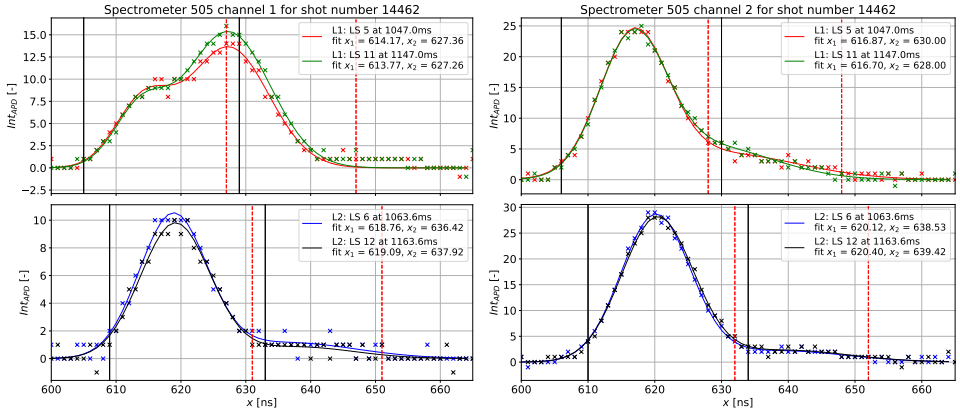

Fig. 4.14: TS data detected by (a) 1. and (b) second channel of polychromator 505 for two laser shots (LS) of each laser (L1,L2) at different times during the plasma discharge. Parameters of the fitting function are not shown to achieve figure clarity.

Considering figures 4.13b and 4.13c, if shown fitted curves are examined in the same way, estimated relative delay Δt_{SL} of the secondary peak is different, namely varies around 13 ns for 3rd channel of spectrometer 506 and from 16 to 20 for its 4th channel. Firstly, this effect could be a result of the fitting routine, due to lower intensity of the secondary light and the fact that it could not be distinguished from the TS signal. Both peaks merges together and more than two Gaussian peaks it resembles an asymmetrical Gaussian with elongated right tail. Even though the double Gaussian function fits the data very well with small deviation, it is not certain that the detected signal is the combination of two Gaussian functions. Further analysis and searching proper function could result in more accurate fitting, and thus the whole diagnostic system.

Examination of laser pulse temporal evolution profile also aids to clarify the shape of detected signal. As a confirmation of such phenomenon, it is useful to measure small portion of laser pulse itself before it enters the tokamak vessel and check if its profile corresponds or resembles afterwards detected signal. Performing this method certainly improves the overall diagnostics reliability and is currently being discussed to be implemented. Possible secondary peaks or non-Gaussian temporal profile of the laser pulse could be detected. To support the fact, that TS signal is asymmetric due to imperfection of laser pulse, it was discovered that the deviation is strictly associated to the detection of the first peak. Once the plasma is terminated, several laser pulses are fired through the tokamak vessel, where none stray light signal is observed. This confirms the statement that the secondary peak is originated when

laser pulse interacts with plasma or is caused by the feature of the APD electric circuit.

On the other hand, this effect also supports the idea that it is caused by stray light, but, rather than unwanted reflection from the beam dump or path, randomly reflected light of the useful signal to the collection optics from inner components of tokamak vessel. Moreover, as seen from 4.14, unambiguous stray light cause by laser misalignment is recorded mostly by first spectral channel. Since this effect is applied for all channels, it suggests similar wavelength range of stray light as the useful signal to be able to reach third and fourth channel.

At this stage, there is no significant evidence for either of proposed hypotheses and further examination and implementation of suggested method to observe output laser pulse temporal evolution is necessary.

4.4.2 Electron temperature and density determination

Assuming the TS signal Int_{TS} in each channel has already been detected, interconnected with proper spatial points and fitted, the integration in the time domain is performed. The integral could be calculated analytically for the case of the Gaussian shape fitting function using

$$I_n = \int_{t_{min}}^{t_{max}} Int_{TS}(n)\,\mathrm{d}t \cong \int_0^{\infty} \mathbf{f}_{1_n}(\mathbf{x})\mathrm{d}\mathbf{x} = \int_0^{\infty} \mathbf{A}_1 \exp\left(-\frac{(\mathbf{x}-\mathbf{x}_{01})^2}{2\sigma_1^2}\right)\mathrm{d}\mathbf{x} = \sqrt{2\pi}\sigma_1\mathbf{A}_1, \tag{4.9}$$

where the standard Gaussian integral for n-th channel was applied. The meaning of variables is explained by (4.8). Boundaries of the integral t_{min} and t_{max} indicates that only the useful data restricted by this range are included during the calculation. From the time integrated TS signal for each polychromator channel, one can easily obtain *Ratios of signal in channels* and *Intensity in channels*. These quantities, which are indicated in the diagram Fig. 4.2, represent the input for the fitting routine, which provides the electron temperature and density evaluation when combined with calibration results. Based on the theoretical background, the Doppler shifted spectrum of the Thomson scattering signal for different temperatures can be determined, see Fig. 2.3. Performing spectral calibration process, when the spectral transmissivity of polychromator channels (Fig. 3.5b) is measured, enables to estimate of ratios of intensities in two following channels (**2 : 1**, **3 : 2**, **4 : 3**) as a function of electron temperature, shown in Fig. 4.3b. As stated above, the electron temperature is dependent od the magnitude of Doppler broadening of the scattered spectrum, which can be reconstructed from the ratios. The total detected intensity of scattered light in all channels is proportional to the electron density when the results from absolute calibration and laser energy measurements are incorporated. In principle, both calculations can be performed individually, but in order to obtain the correlation matrix, which is subsequently used for the estimation of pressure, both calculations are performed simultaneously during one fitting procedure, but are separated in the diagram to maintain simplicity.

The process of fitting the measured intensities in all channels of each polychromator, consists in simulating the Thomson scattering spectrum for given electron

temperature T_e and density n_e, overlapping obtained spectrum over the spectral transmissivity function of each polychromator channel and integrating transmitted intensity. Once this is performed, the intensities in all channels of a given polychromator are obtained. The simulated intensities are then compared with the measured ones. Implemented fitting function incorporates in its core the function *curve_fit* from the Python Scipy package[30], which is based on non-linear least squares method. The fitting process consists in minimization the sum of squares of given datasets. In this case, the two data sets are the calculated and measured intensities in the four polychromator channels.

Last stage of the data processing algorithm consists in assigning calculated values to the right time and position. Results from spatial calibration are used to assign measured data to tokamak **z-axis** position. For temporal assignment laser shot trigger time marks from ATCA2 are used. Overall result of the data processing unit of TS diagnostics on the COMPASS tokamak consists in data sets containing profile of electron temperature T_e and density n_e as a function of vertical position along the laser beam axis (**z_axis**) for each relevant laser shot during the plasma discharge.

Fitting function was successfully implemented to the data processing algorithm and its performance is presented below on two measurements during different phases of one tokamak discharge #16832. Fitting of each measurement is presented with three figures. Graphs on the top indicate the measured intensity by all four channels of given polychromator, 510 (a) and 527 (b), which observe central (z=0.01 m) and edge (z=0.23 m) positions in the plasma, respectively. In both cases Fig. 4.15c and Fig. 4.16c different ratios of intensities detected by polychromator channels can be observed. Both measured and fitted intensities are shown in the graphs. The polychromator 510 observes the plasma core region, where higher temperature and density are anticipated in comparison to the plasma edge region, which is observed by the second polychromator 527. Presented signal intensities in Fig. 4.15a and Fig. 4.15b are in good agreement with the assumption. As mentioned above, the shift of the peak of the spectrum towards the lower wavelengths increases with the electron temperature, while the intensity is proportional to the electron density. Since the channel numbering is consistent with Fig. 4.3a, the fact that the signal in the third and fourth channel of the polychromator 510 is larger than in the first two, signifies larger shift of the spectrum towards the shorter wavelengths, thus larger temperature, than in the case of the polychromator 527. The intensity detected by the two polychromators is significantly different, but the impact on the fitted electron density is not so noticeable. One must remember that the density determination is related to the results of absolute calibration. From the Raman factor presented in Fig. 4.7 can be noticed that the Raman factor value in the core region is more than twice as large as the intensity in the edge. This signifies that for the same electron density the edge polychromators will measure substantially lower intensity than the core ones, due to the shorter scattering length.

In the bottom graph (c) the full profile of electron temperature T_e, density n_e and pressure p_e calculated for each of the two measurements. The profile of the plasma pressure p_e can be determined as a product of the temperature and density. The errors of the measured data are calculated from the errors of fitting fast signal and resulting from absolute calibration by means of Raman scattering. These errors are used as

inputs for the electron temperature and density fitting function. Simultaneously with the fitted parameters, the covariance matrix is received, from which the errors of temperature, density and also pressure can be calculated.

In order to validate the results of the newly implemented data processing system, a comparison with the IDL implementation is provided. Full profiles of electron temperature, density and pressure are overlapped in Fig. 4.15. As can be seen the profiles of temperature and density are in very agreement along the whole observed region, while values calculated with Python are systematically lower, which is more apparent from the pressure profile since the discrepancies are multiplied. The reason for this systematic difference remains uncertain, however, it can be explained by the different fitting function of the fast signal, presented in Fig. 4.12, which effectively lowers the intensity of the useful signal. Proper analysis of the impact of the new fitting function has to be provided. One can also notice, that profiles calculated using IDL are missing several point within, where the fitting routine failed, while the new routine successfully evaluated the whole profile.

The data processing system is presented for one more measurement during the same discharge in Fig. 4.16. Similar observations as in the previous case can be provided, when the top two graphs are examined. However, significantly higher intensities are measured, which results in considerably higher electron density. Increase in the electron density is also evident from the full profile calculation. The region with the steep gradient present in the edge region at z=0.26-0.28 m is called pedestal and it appears when the plasma transits to a different regime called high-confinement mode or H-mode [31]. Also in this particular discharge, the new data processing system is proven to calculate resembling values of electron temperature and density with the same systematic difference from the IDL processing routine as in the previous case, which needs to be investigated.

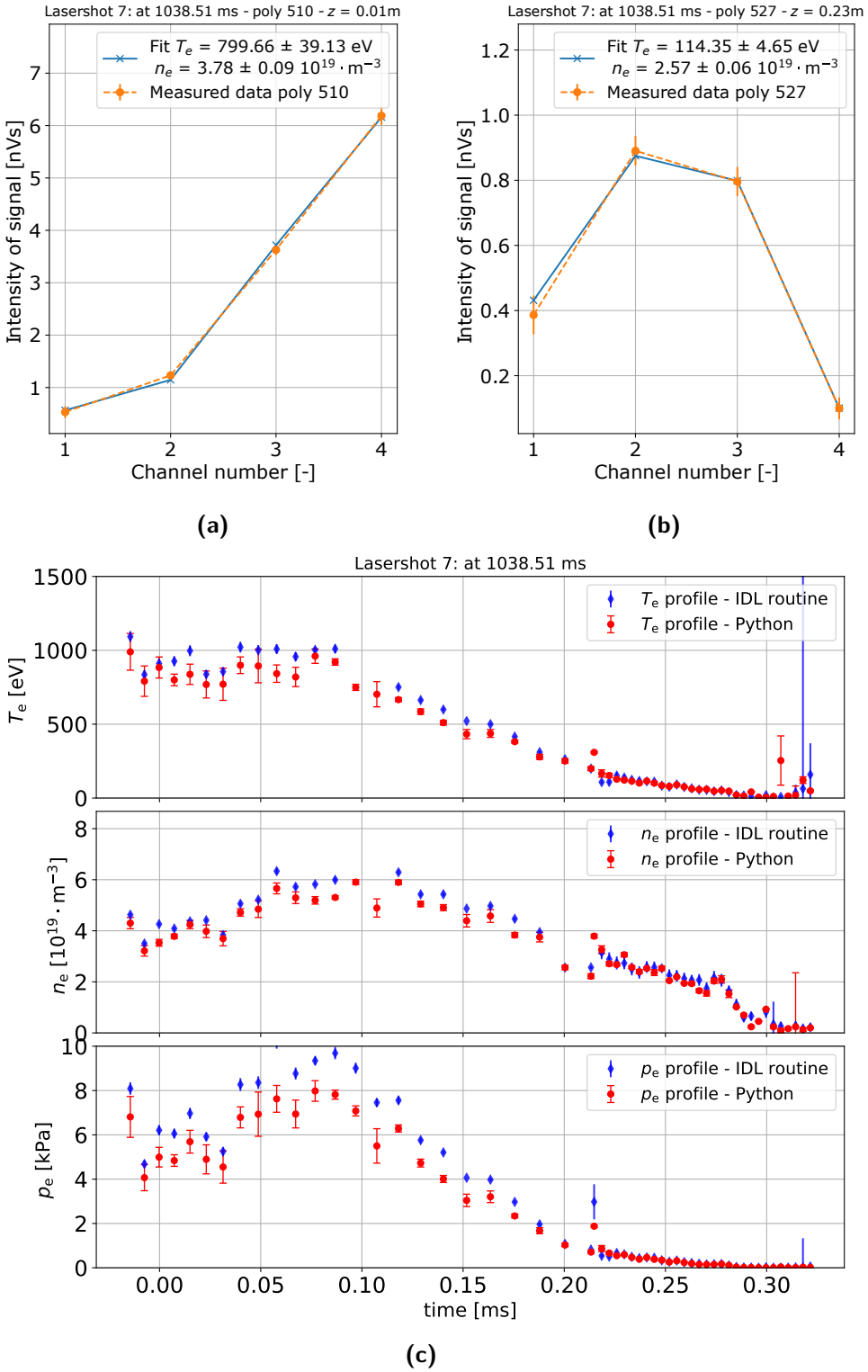

Fig. 4.15: Fitting of the measured intensity by all four channels of polychromators (poly) (a) 510 at $z = 0.01$ m and (b) 527 at $z = 0.23$ m measured at 1038.15 ms during the tokamak discharge #16832. (c) Full profile calculation of electron temperature T_e, density n_e and pressure p_e. Comparison between IDL routine and Python provided.

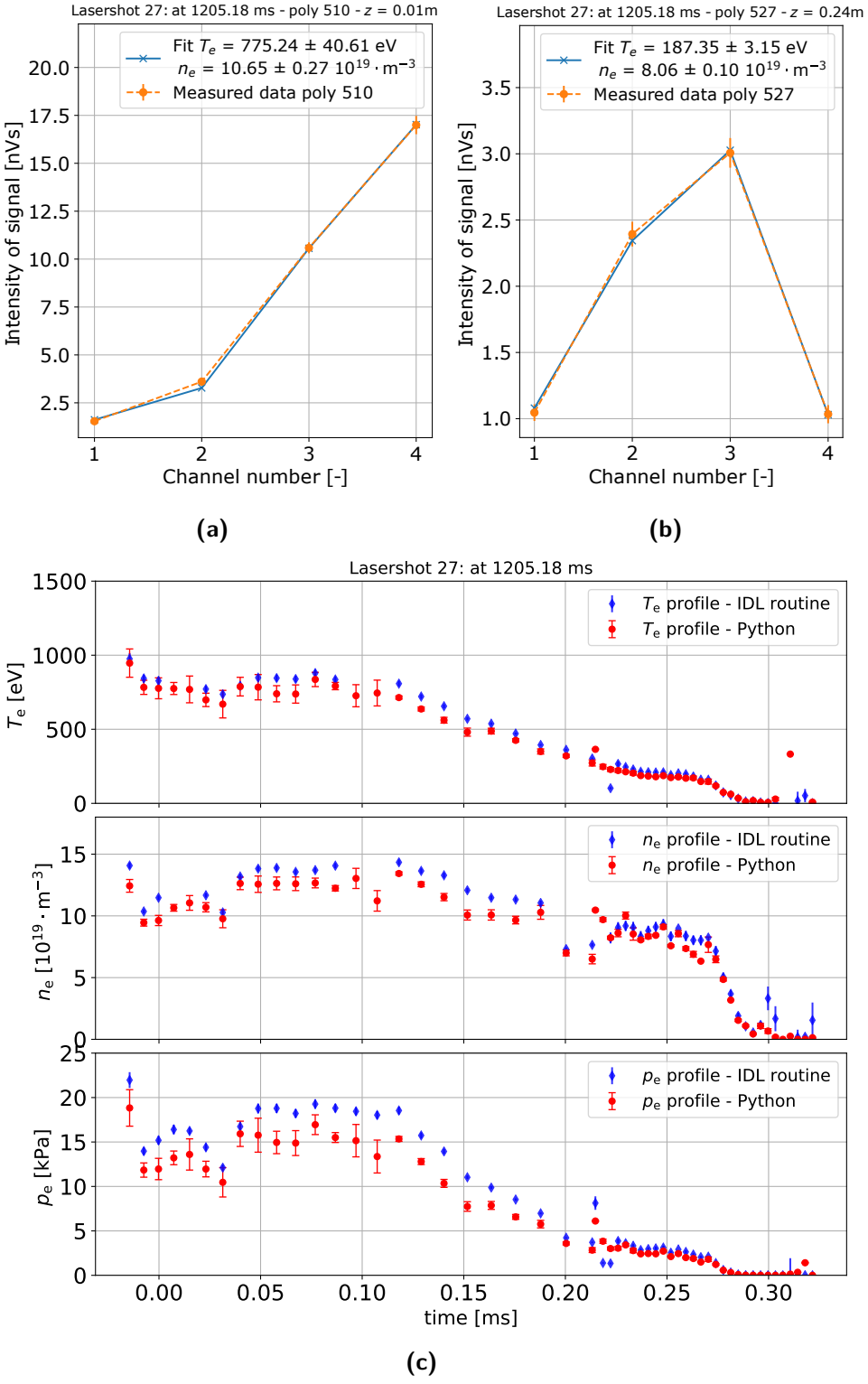

Fig. 4.16: Fitting of the measured intensity by all four channels of polychromators (poly) (a) 510 at $z = 0.01$ m and (b) 527 at $z = 0.23$ m measured at 1205.18 ms during the tokamak discharge #16832. (c) Full profile calculation of electron temperature T_e, density n_e and pressure p_e. Comparison between IDL routine and Python provided.

Chapter 5

Means of alignment of the optics with respect to the laser beam

In the following chapter the author's contribution at 22nd Topical Conference on High Temperature Plasma Diagnostics on April 2018 is presented. Poster and paper subscription, which were prepared in the course of making this diploma thesis, are presented to extend its scope, since it would not be possible to carry out the contribution without adopted knowledge and accomplished advances within the preparation of the thesis. The topic concerns evaluation of means of alignment of the optics with respect to the laser beam, which is the crucial concern for the spatial calibration of the Thomson scattering diagnostic system and reliability of provided measurements. If the whole cross-section of the beam is not imaged onto the detector input, the collected light intensity drop is interpreted as a decrease of the electron density, in the worst case the measurement is impossible. The lower signal also increases the statistical error of the temperature measurement. A tool for alignment evaluation is therefore necessary. It helps during installation and preparation of the TS system, during measurements it serves as a feedback tool for either validation of the measurement or even as an input for active alignment correction system. Particular information is already presented above, but here repeated to maintain consistency and provide comprehensive independent chapter.

5.1 Laser and optics alignment

A commonly used alignment-checking method is the observation of the ratio of signals collected from different segments of the fibre bundle. One particular implementation of this method is referred to as "split-fibre" - the bundle of the fibres collecting the light from one spatial point of the TS system is divided into halves along the laser beam propagation direction [27, 29]. Any deviation of the signal ratio from unity indicates the laser beam image is not in the middle of the fibre bundle. When light from both split-fibre halves is detected in polychromators and the signals are added, the electron temperature and density can be evaluated in this spatial point as is done for the signal acquired by other fibre bundles.

Another implementation of alignment evaluation requires extra fibres mounted on the sides of the regular fibre bundles used for TS light collection - the method

can be called "side-fibre", it is used, for instance, on NSTX-U[28]. If the laser beam is misaligned, the wings of its profile reach out to the side-fibre and some signal is detected in the alignment fibre. Contrary to the split-fibre, the side-fibre signal is usually not evaluated for electron temperature and density, and additional detection of the side-fibre signal is required. Usually a single channel detector equipped with a suitable filter is sufficient for such detection and easier to implement.

Theoretically, a design with three regions in the fibre bundle could be a variation of the side-fibre method with the advantage of summing all signals for TS evaluation, i.e. without discarding any collected light. But any further splitting of collected light increases the statistical error of its detection, calling the original advantage into question.

5.2 Simulation of split fibres

The split-fibre method plays a key role during the alignment process of the Thomson scattering diagnostic on COMPASS. In order to optimize this technique, a simulation of the Thomson scattering signal detected by a split-fibre bundle was carried out for various arrangements of fibres within the fibre bundle. Profile of the laser beam which is used for the TS diagnostic on the COMPASS tokamak varies between the Gaussian and Top-hat shapes along the beam path, therefore, both shapes were used in the simulation. Existing fibre bundle arrangement[24] of the core and edge TS system on the COMPASS tokamak can be found in Fig. 5.2. The spatial resolution is determined by the fibre bundle size and collection lens magnification. According to the requirements for the spatial resolution in the edge and core plasma regions the orientation of the longer side of the fibre bundle was set perpendicular and parallel to the laser beam propagation direction, respectively.

The scattered light originating from the plasma is focused by the collection optics on the fibre bundles. It can be assumed that the scattered light profile corresponds to the laser beam profile. In order to obtain the projection of the laser beam on the fibre bundle it is integrated along the line of sight, which is shown for the Gaussian shape in Fig. 5.1a. The result of the projection on the whole fibre bundle is demonstrated in Fig. 5.1b. The x and y axes are in the plane of the fibre bundle perpendicular and parallel to the laser beam propagation, respectively, while the z-axis is in the direction of the fibre bundle's line of sight.

5.2.1 Fibre bundle throughput function

Scattered light imaged onto the bundle is collected by individual fibres and transmitted towards the detection unit outside the tokamak hall. The simulation of the efficiency of light collection of one fibre bundle requires to move the projected function along the x-axis and record the amount of the collected signal at each position. Since it can be assumed the laser beam is co-linear with the y-axis (or very close to co-linear) within the fibre bundle, the profile is expected to be the same along the y-axis and the problem can be reduced to one dimension using a so called *throughput*

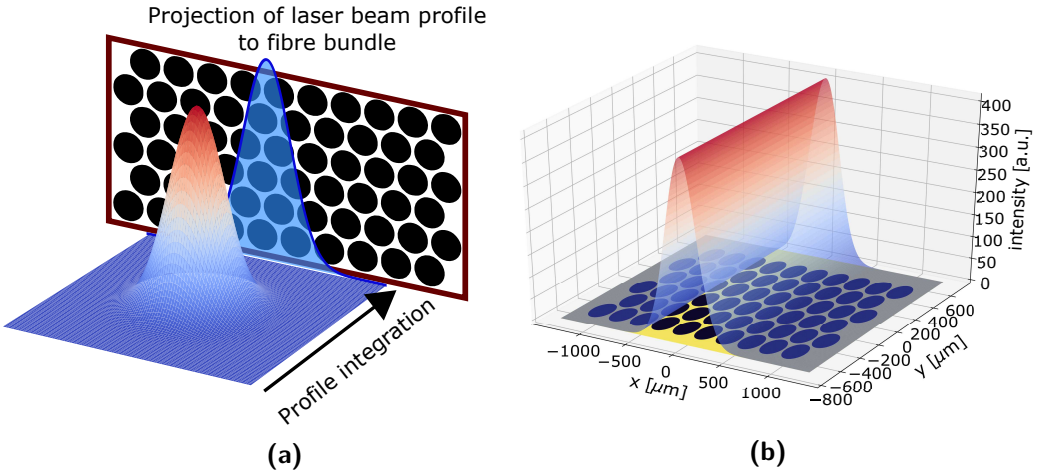

Fig. 5.1: (a) The Gaussian laser beam projection into the plane of the fibre bundle, (b) projection of the integrated Gaussian beam on the whole fibre bundle.

function f_T, which is given by the bundle geometry. It can be calculated from the bundle image or analytically using the following function

$$f_T(x) = \sum_{x_i \in S} 2\sqrt{r^2 - (x - x_i)^2}, \tag{5.1}$$

where x_i represents the i-th fibre centre position on the x-axis (horizontal) from a given set of fibres S with the fibre radius r. The formula for f_T is derived by integrating the fibre (circle) along the y-axis. The throughput function for the current edge TS split-fibre bundle is shown in Fig. 5.2, for each segment of the split-fibre separately, together with the typical beam shape profiles projected on the fibre bundle of a width corresponding to Tab. 5.1. The Gaussian profile width at $1/e$ of the amplitude is equal to the width of the Top-hat function.

5.2.2 Simulation

The estimated laser beam size on COMPASS TS in the toroidal direction, along the x-axis, is presented in Tab. 5.1. Vertical positions correspond to those observed by the split-fibres. The magnification of the optical systems is 0.34 and 0.35 for the core and edge TS, respectively [29], and was used to estimate the width of the scattered signal on the split-fibre bundles, written in the last row of the table. Values were extrapolated from the diameter measurements during a commissioning phase [32].

In order to evaluate the split-fibre performance, the beam function is moved along the x-axis and the signal acquired by a corresponding split-fibre bundle segment is recorded. Both the total acquired signal and the ratio of signals in particular segments can be examined. From the former the signal loss can be determined and the latter can be used to assess the beam position on the bundle, thus serving as an alignment tool.

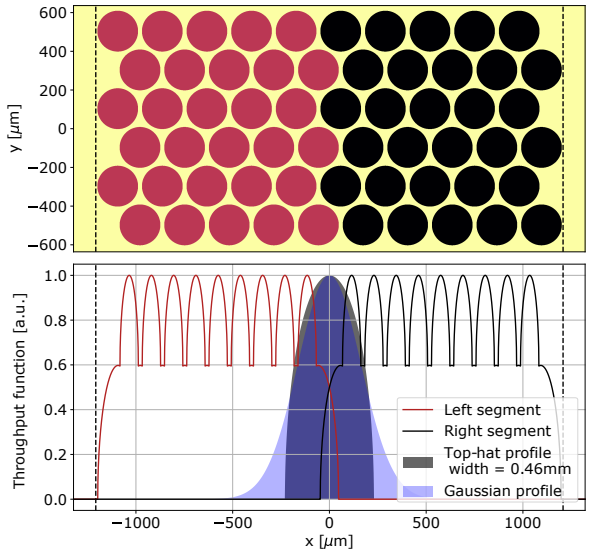

(a) Edge TS split-fibre bundle

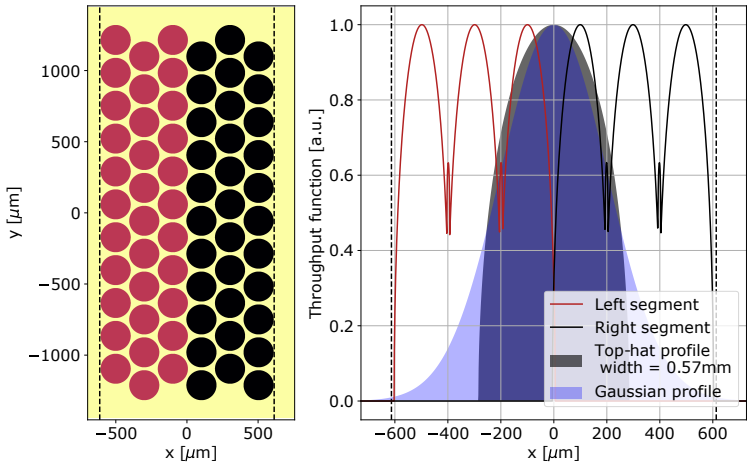

(b) Core TS split-fibre bundle

Fig. 5.2: The fibre bundle with highlighted halves of split-fibre (top,left). Corresponding throughput functions and beam profiles are shown (bottom,right)

5.2.3 Results

The results of simulation of the split-fibre performance are presented in two steps. Firstly, the current status of the method on COMPASS TS is evaluated and afterwards alternative approaches with possible upgrades are proposed.

Performance of the current approach

In Fig. 5.3 the total acquired signal is shown for both the edge and core split-fibres, where values $T_G^{10\%}$ and $T_T^{10\%}$ represent the value of the beam centre displacement corresponding to the 10% threshold of useful signal loss for the Gaussian and Top-hat

Split-fibre	Edge		Core	
Vertical position	277	215	187	-14
Beam width in vessel	1.32	1.54	1.68	3.10
Beam width at fibre d	0.46	0.54	0.57	1.05

Tab. 5.1: The laser beam size in the toroidal direction at the vertical position (over mid-plane) observed by the split-fibre after being focused into the vessel. Values are in mm.

shapes, respectively. In general, the edge TS fibre bundle is more resistant to the beam displacement, as $T_{G,T}^{10\%} \approx 1$ mm, while for the core TS this value decreases, in the plasma centre even down to 0.25 mm. This is the result of the different geometry of the fibre bundles for the core and edge TS and, additionally, of the laser being focused on the plasma edge region, due to higher requirements on the spatial resolution in this region.

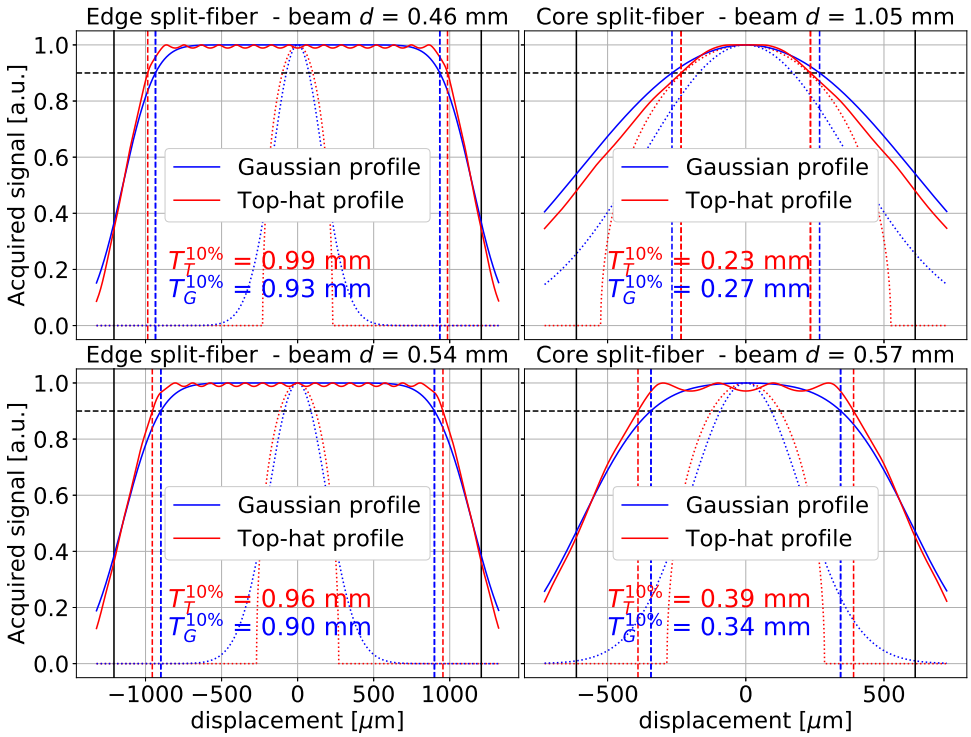

Fig. 5.3: The total acquired signal while the beam function (Gaussian,Top-hat) is moved along the x-axis. Black vertical lines highlight the split-fibre boundaries. The horizontal dashed line represents the 10% threshold of signal loss, which is exceeded when the Gaussian or Top-hat beam is shifted over $T_G^{10\%}$ or $T_T^{10\%}$, respectively.

The current COMPASS TS diagnostic includes 4 split-fibres divided vertically in two identical halves as shown in Fig. 5.2. Ratios of signals acquired by these particular segments are shown in Fig. 5.4 as a result of the same simulation. The reddish region indicates the measurable range of the analog-to-digital converter (ADC) used to digitize the signal with a resolution of 8 bits, therefore, ratios outside

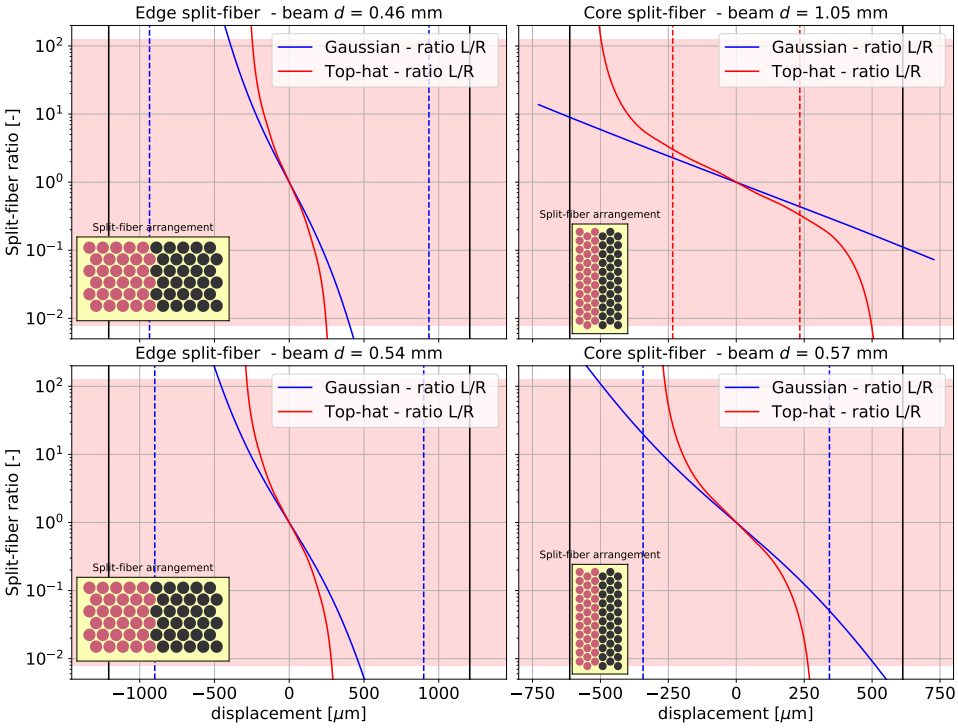

Fig. 5.4: The simulated split-fibre signal ratio for a given beam profile and split-fibre arrangement. The reddish region represents the ADC resolution (8-bit).

the range (1 : 128, 128 : 1) are unfeasible to record. This range is certainly overestimated as signal noise has to be considered. The edge split-fibre ratio shows that the beam displacement of less than 0.5 mm causes the ratio to exceed the measurable range and become unusable as a tool for alignment, despite the fact that there is no significant signal loss. On the other hand, in the core region one could benefit from the split-fibre ratio as it remains in the measurable range even for a significant displacement. However, in this case the signal loss is noticeable, therefore, for the core TS on the COMPASS tokamak it is advisable to keep the ratio as close to unity as possible.

The measured signal ratio with four split-fibres is presented in Fig. 5.5a(top) for the discharge #15978. Using the split-fibre simulation the dynamic of the ratio can be quantified and the corresponding displacement can be calculated, which is presented in the bottom part of the same figure. As can be seen, the calculated displacements within each of the core and edge TS are correlated both in amplitude and temporal evolution. This suggests that the beam is moving similarly across both split-fibres within core and each TS. This supports the idea that the significant displacement especially in the core region is the result of the collection optics displacement rather than a laser beam misalignment. Calculated displacement is shown individually in Fig. 5.5b. Two green regions represents 1σ and 2σ widths of the Gaussian beam, which correspond to 68% and 95% of the acquired signal, respectively. Horizontal dashed lines mark the boundary of the fibre bundle. In the edge TS the results indicate a relatively small displacement within the bundle. For the core TS, where

the beam is significantly wider, the displacement is larger and in both cases partly reaches out of the fibre bundle area. Most significant displacement occurs during the initial phase of the discharge. Such misalignment results in non-negligible signal loss.

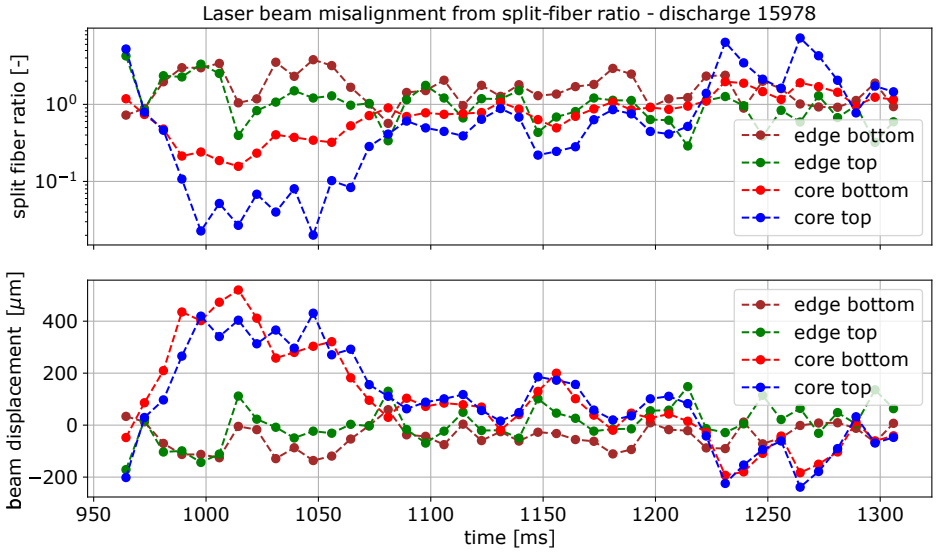

(a) The split-fibre ratio during discharge #15978.

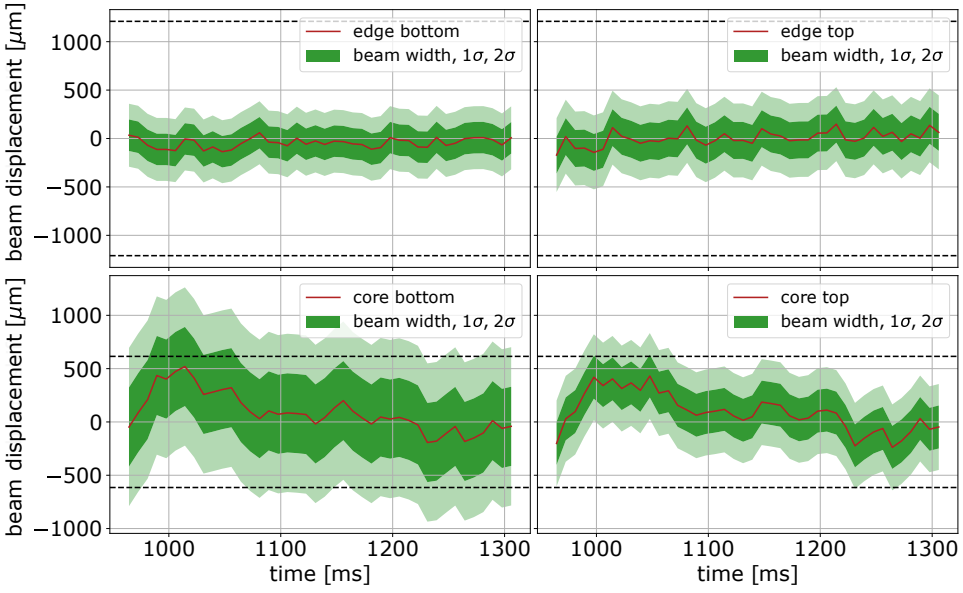

(b) The beam displacement on the split-fibre bundle reconstructed from the measured split-fibre signal using the simulation.

Fig. 5.5: The beam movement reconstruction.

Alternative approach

The steep evolution of the split-fibre ratio exceeding the measurable range limit in the edge TS case is the result of the beam profile being narrow enough to fit entirely onto one half of the split-fibre. Therefore, dividing the fibre bundle vertically is not an optimal solution. Alternative approaches are evaluated within this section. Simulations are performed for the beam size of $d = 1.05$ mm and 0.46 mm for the core and edge fibre bundle arrangements, respectively. The signal loss dependence on the displacement is the same as in Fig. 5.3 for a given laser beam and fibre bundle width. Results are presented in Fig. 5.6 for different fibre bundle arrangements. The level of 10% signal loss is shown by vertical dashed lines. The split-fibre arrangement is shown at a miniature scale within each graph.

The signal ratio for the diagonal arrangement of the split-fibre bundle for the edge and core TS is shown in the Fig. 5.6a. As seen in the figure, in the left (edge plasma) case the whole measurable range is fully utilized even for a large displacement, making it a superior variant. On the other hand, the diagonal arrangement for the core TS does not provide better utilization of the ratio's measurable range compared to the current approach, therefore, the vertical distribution is more applicable in this case. Nevertheless, the ratio for the two presented beam profiles has a similar dynamic in comparison to the vertical arrangement, where the ratio diverges for the Top-hat shape. This could provide a valuable benefit for the case when the beam profile is not definite. In Fig. 5.6b different diagonal distributions of the fibres within the bundle are shown. The inclination of the line dividing the fibre bundle in two halves has a significant impact on the ratio dynamic. The arrangement in Fig. 5.6b (left) shows a rather slow gradual dynamic of the ratio even beyond the 10% signal loss limit, which would not be suitable for the detection of a large misalignment. In contrast, in the variant on the right of the same figure the ratio rises rapidly as it approaches the 10% signal loss limit and the arrangement would be even more convenient as a substantial misalignment is detected before the significant signal loss occurs.

The results in Fig. 5.6c for the side-fibre method show that it provides a comparable tool for alignment, as the ratio is well quantifiable in the region close to the 10% limit, for both the core and edge cases. However, this technique requires a more detailed optimization process considering either signal loss or including additional detectors designated for alignment purposes only.

5.3 Correlation with vibration measurements

In order to investigate the effect of vibrations, four 3-axis accelerometers (ADXL335) were mounted on the components of the TS diagnostics. Different locations, which are assumed to be crucial for the alignment, were selected (collection lenses, fibre holders, tokamak port). Accelerometer measurements are synchronized with the tokamak discharge and the data is collected during a proper time period with a sampling frequency of 12 kHz. The examination of correlation with vibration measurements was mainly motivated by the fact, that the core and edge TS shows similar evolution of the split-fibre ratios for different discharges, which is presented

in Fig. 3.4. This observation initiated the investigation of potential systematic sources of such undesirable effect, which can decrease the reliability of the diagnostic system.

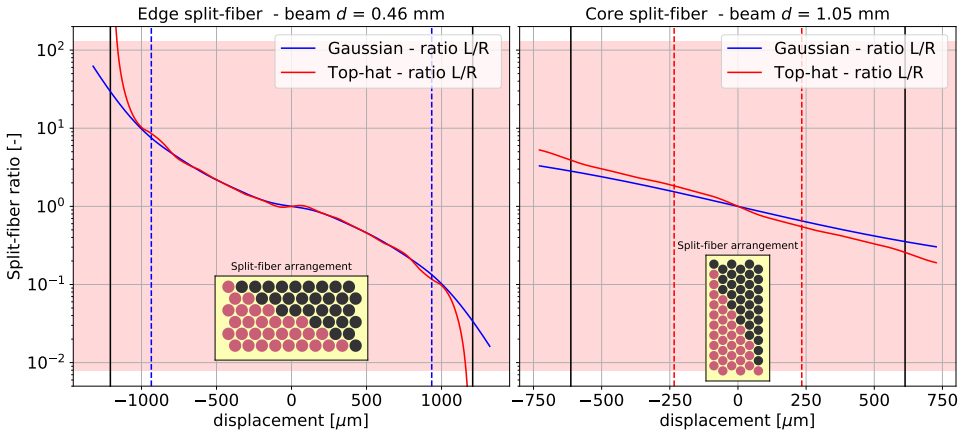

(a) The diagonal arrangement

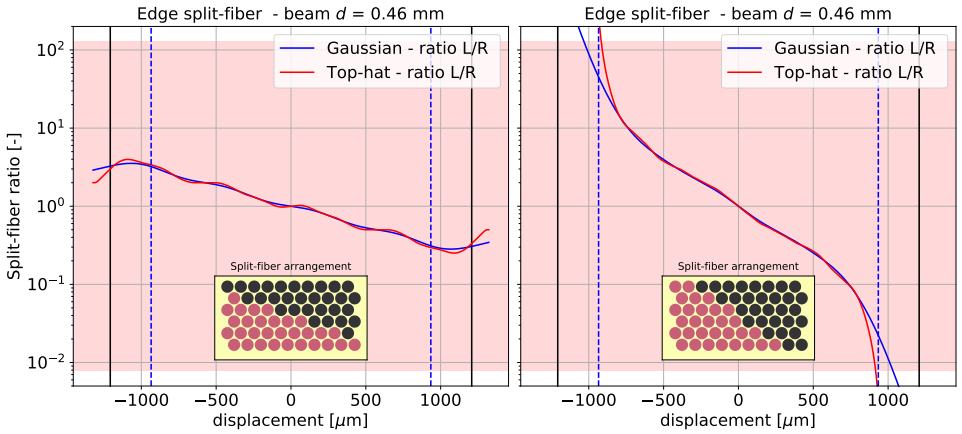

(b) Diagonal arrangement variations - edge split-fibres

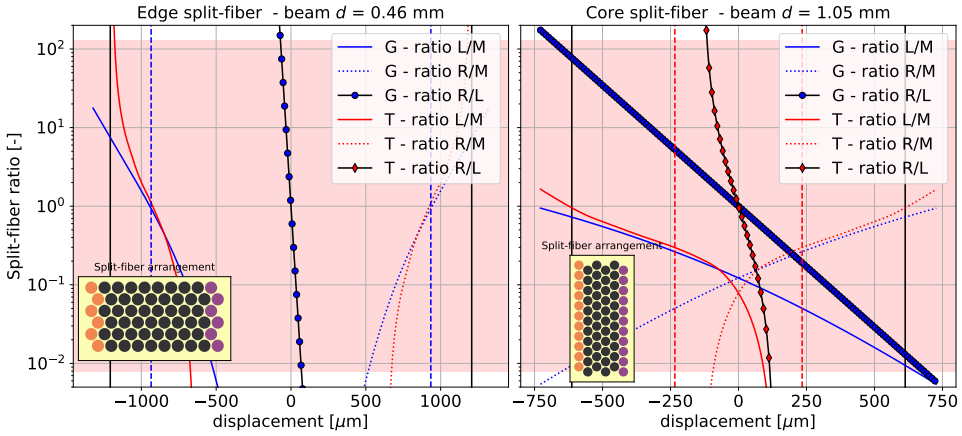

(c) Three vertical segments - side-fibres

Fig. 5.6: The simulated signal ratio for various fibre arrangements of both the core and edge TS.

The measurements of vibrations at all positions show a high level of reproducibility for discharges with similar global parameters, namely the plasma current I_p and the toroidal magnetic field B_T, which is presented in Fig. 5.7a for three discharges. In order to calculate the displacement Δ, the acceleration a is twice integrated with respect to time, while a high-pass filter was used to reduce the undesirable trend resulting from integrating a non-zero offset. Spectrograms of both acceleration and displacement are shown in the background of Fig. 5.7a for the discharge #15978. In the beginning of the discharge higher frequency $\sim$ 100 Hz oscillations appear. This indicates an initial "kick" during the plasma ramp-up. Afterwards the frequency decreases as the mounted structure begins to vibrate with a characteristic frequency of approximately 20 Hz.

The calculated displacement from accelerometers and results from the split-fibre method, presented in Fig. 5.5a, are compared for the discharge #15978 in 5.7b. A linear trend from split-fibre results was removed as this is impossible to record using the accelerometer measurement, due to the undesirable offset. A similar oscillation character as in Fig. 5.7a(bottom) is present also in the split-fibre measurement. The results are in good agreement both in the amplitude and the frequency of approximately 20 Hz. This suggests that the vibrations of the collection lens structure are responsible for the oscillation of the split-fibre ratio signal.

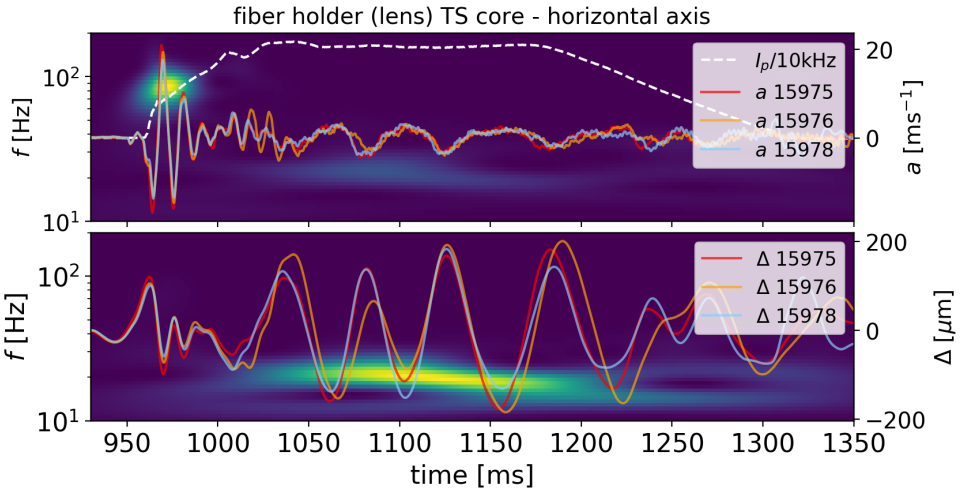

(a) Spectrograms of measured acceleration a (top) and calculated displacement Δ (bottom) on the core TS fibre holder.

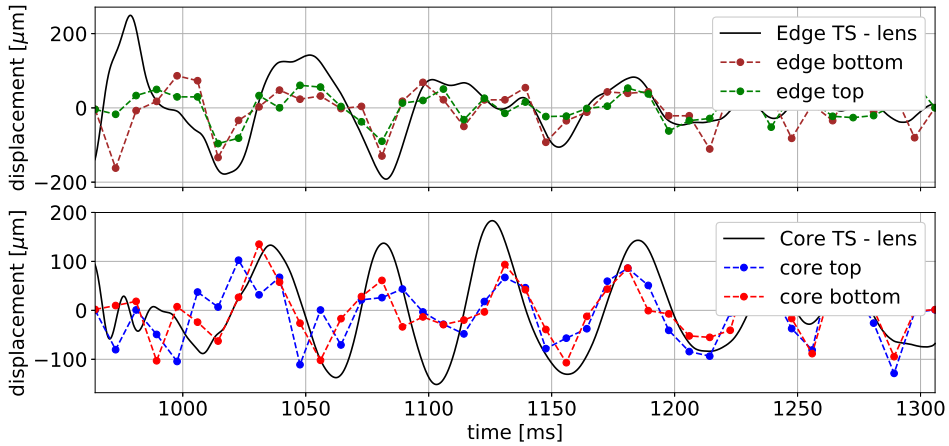

(b) The correlation of the calculated displacement from the split-fibre method and the vibration measurement.

Fig. 5.7: Displacement evolution for discharge #15978.

Chapter 6

Conclusions

This thesis concerns several aspects related to the diagnostics based on the Thomson scattering, which is the key diagnostics used on tokamaks. Within chapter 2 in Part I the theoretical principles of plasma physics and Thomson scattering are presented. In chapter 3 the realization of this diagnostic is illustrated on the one integrated on the COMPASS tokamak. All of the presented results and implementations have been performed for the Thomson scattering diagnostic on the COMPASS tokamak.

The thesis assignment is divided into two separate parts: the first one consists in implementing a new set of routines for data processing and the second concerns the spatial calibration method improving the diagnostics alignment.

The key task of this thesis was to develop and implement an entirely new set of routines in open source programming language Python to substitute the current version provided in IDL language. In chapter 4, the entire data processing system was described, divided into partial segments and analysed in order to obtain insight to the core of the whole process and to reveal inputs contributing to the calculation. Based on the drawn up flow chart the individual subsystems were implemented.

Suggested improvement of the fitting procedure of the raw TS signals was to fix some of the fitting parameters. Output of the absolute calibration by means of Raman scattering was assessed as a source of desirable initial values. This method was finally proven to be inapplicable due to the fact, that the fitted parameters were variable to larger extent than expected. Nonetheless, the whole process of absolute calibration was implemented together with various optimization approaches, which enabled almost fully automated processing. The calculated results of the Raman factor showed very good agreement when compared with the results of original IDL routines.

Double Gaussian fitting function, which better reproduces the curve of the detected signal, was proposed as the new fitting function. Using this technique, signals otherwise corrupted by stray light could be restored. The data processing part was completed by the determination of the electron temperature and density profiles. The calculated profiles of the temperature and density are in good agreement with the results from the original IDL routine, while the systematic difference of both parameters is observed. Possible explanation was provided and needs to be verified. The stability and the robustness of the newly implemented data processing system was proven to be improved.

Before the implementation of the system as a standard tool for the Thomson scattering data processing, a proper validation and testing must be provided. The most reliable method to verify the system accuracy and reliability is to introduce simulated noisy data of known parameters to the system and perform fitting procedure. By comparing the results with the parameters of the simulated signal the system performance could be evaluated. These tests are being prepared.

The last task of the first part of the thesis assignment, includes saving the results to the COMPASS tokamak database. Since the performance of the newly implemented set of routines is not properly verified and tested, there is no reason to save the results to the database. Nevertheless, during the preparation of this thesis, the author obtained valuable experience with the COMPASS database. Therefore, the process of saving the data to the database and making the newly implemented system a standard processing unit for the Thomson scattering diagnostic can be performed promptly once the commissioning phase has ended.

The well established alignment methods based on "split-fibres" and "side-fibres" were described and compared in chapter 5. It was shown that the "split-fibre" bundle arrangement can be optimized for the particular laser width and the fibre bundle width. Such optimization can be interesting for future TS systems for tokamaks like COMPASS-Upgrade[33] or ITER. Besides this analysis, the practical use of split-fibres on the COMPASS tokamak was presented, reconstructing the evolution of the laser beam image position on the fibre bundle during the tokamak discharge. This feature can be used to quantify the amount of the useful signal loss during the standard tokamak discharge measurement. At some extent such information could provide the correction of the density measurement. It would enhance the accuracy and reliability of the TS diagnostics if implemented successfully and applied routinely during the post processing. It was proven that the measured split-fibre ratio is in good agreement with the collection lens vibrations measurement. Results and advancements obtained within the last chapter were presented at 22nd Topical Conference on High Temperature Plasma Diagnostics in April 2018 and the manuscript was handed over for the submission process in May 2018.

Appendices

Appendix A

Index

Appendix B

Bibliography

[1] J. D. Lawson. *Some criteria for a Power producing thermonuclear reactor (Technical report)*. Atomic Energy Research Establishment, 1955. Harwell, Berkshire, U.K.

[2] K. Miyamoto. *Plasma Physics for Controlled Fusion*, volume 92 of *Springer Series on Atomic, Optical, and Plasma Physics*. Springer-Verlag Berlin Heidelberg, 2016. ISBN: 978-3-662-49780-7.

[3] J. Wesson. *Tokamaks*. Oxford Engineering Science Series. Oxford University Press; 2 edition, 1997. ISBN: 9780199592234.

[4] P. Kulhánek. *Úvod do teorie plazmatu*. AGA (Aldebaran Group for Astrophysics), 2011. ISBN 978-80-904582-2-2.

[5] W. Crookes. *On radiant matter, A lecture delivered to the British Association for the Advancement of Science, at Sheffield, Friday, August 22, 1879 /*. London :[s.n.],.

[6] Institute of Plasma Physics of the CAS. COMPASS tokamak. `http://www.ipp.cas.cz/vedecka_struktura_ufp/tokamak/tokamak_compass/`. [Online; accessed 12/1/2017].

[7] Max-Planck-Gesellschaft. Introduction: the ASDEX Upgrade tokamak. `http://www.ipp.mpg.de/16208/einfuehrung`. [Online; accessed 12/1/2017].

[8] EUROfusion. JET's main features. `https://www.euro-fusion.org/jet/jets-main-features/`. [Online; accessed 12/1/2017].

[9] ITER Organization. ITER - the way to new energy. `https://www.iter.org/`. [Online; accessed 12/1/2017].

[10] S. L. Prunty. A primer on the theory of Thomson scattering for high-temperature fusion plasmas. *Phys. Scr.*, 89, 2014.

[11] J. Sheffield, et al. Plasma scattering of electromagnetic radiation. *Academic Press*, 2011. Burlington, USA, ISBN 978-0-12-374877-5.

[12] A. C. Selden. Simple analytic form of the relativistic thomson scattering spectrum. *Physics Letters A*, 79(5):405 – 406, 1980.

[13] David W. Hahn. Raman scattering theory. University of Florida, 2007.

[14] B. P. LeBlanc. Thomson scattering density calibration by rayleigh and rotational raman scattering on nstx. *Review of Scientific Instruments*, 79(10):10E737, 2008.

[15] R. Scannel. *Investigation of H-mode edge profile behaviour on MAST using Thomson scattering*. PhD thesis, 2007.

[16] M. Aftanas, et al. Thomson scattering on COMPASS - commissioning and first data. *JINST*, 7(C01074), 2012.

[17] C. M. Penney, R. L. St. Peters, and M. Lapp. Absolute rotational raman cross sections for n2, o2, and co2. *J. Opt. Soc. Am.*, 64(5):712–716, May 1974.

[18] St. C. McCool. Calibration of thomson scattering measurements. *FRCR No. 242*, 1982.

[19] G. Vaughan, D. P. Wareing, S. J. Pepler, L. Thomas, and V. Mitev. Atmospheric temperature measurements made by rotational raman scattering. *Appl. Opt.*, 32(15):2758–2764, May 1993.

[20] P. Böhm. *Temporally and spatially resolved evolution of plasma in the COMPASS tokamak*. PhD thesis, Czech Technical University in Prague, Faculty of Nuclear Sciences and Physical Engineering, 2011.

[21] P. Bilkova, P. Bohm, M. Aftanas, M. Sos, A. Havranek, D. Sestak, V. Weinzettl, M. Hron, R. Panek, the COMPASS team, and the EUROfusion MST1. High resolution thomson scattering on the compass tokamak—extending edge plasma view and increasing repetition rate. *Journal of Instrumentation*, 13(01):C01024, 2018.

[22] R. Scannell, et al. Design of a new Nd:YAG Thomson scattering system fot MAST. *Rev. Sci. Instrum.*, 79(10E730), 2008.

[23] R. Scannell, et al. A 130 point Nd:YAG Thomson scattering diagnostic on MAST. *Rev. Sci. Instrum.*, 81(10D520), 2010.

[24] P. Bilkova, et al. Design of new Thomson scattering diagnostic system on COMPASS tokamak. *Nucl. Instrum. and Meth. in Phys. Res. A*, pages 1273–1276, 2010.

[25] M. Sos. *Tokamak plasma diagnostic based on Thomson scattering - calibration*. Bachelor thesis, Czech Technical University in Prague, Faculty of Nuclear Sciences and Physical Engineering, 2015.

[26] M. Tripsky. *Calibration of polychromators adn using them for diagnostics of Thomson scattering*. Bachelor thesis, Czech Technical University in Prague, Faculty of Nuclear Sciences and Physical Engineering, 2011.

[27] J. Figueiredo, G. Naylor, M. Walsh, M. Dunstan, R. Scannell, and F. Serra. Mast yag thomson scattering upgrade alignment system. *Review of Scientific Instruments*, 81(10):10D521, 2010.

[28] B. P. LeBlanc and A. Diallo. Alignment of the thomson scattering diagnostic on nstx. *Journal of Instrumentation*, 8(11):C11004, 2013.

[29] P. Bilkova, P. Bohm, M. Aftanas, M. Sos, A. Havranek, D. Sestak, V. Weinzettl, M. Hron, R. Panek, the COMPASS team, and the EUROfusion MST1. High resolution thomson scattering on the compass tokamak—extending edge plasma view and increasing repetition rate. *Journal of Instrumentation*, 13(01):C01024, 2018.

[30] The SciPy community. ScipPy 1.1.0 Reference guideline. `https://docs.scipy.org/doc/scipy/reference/generated/scipy.optimize.curve_fit.html#scipy.optimize.curve_fit`. [Online; last accessed 1/5/2018].

[31] F. Wagner, G. Becker, K. Behringer, D. Campbell, A. Eberhagen, W. Engelhardt, G. Fussmann, O. Gehre, J. Gernhardt, G. v. Gierke, G. Haas, M. Huang, F. Karger, M. Keilhacker, O. Klüber, M. Kornherr, K. Lackner, G. Lisitano, G. G. Lister, H. M. Mayer, D. Meisel, E. R. Müller, H. Murmann, H. Niedermeyer, W. Poschenrieder, H. Rapp, H. Röhr, F. Schneider, G. Siller, E. Speth, A. Stäbler, K. H. Steuer, G. Venus, O. Vollmer, and Z. Yü. Regime of improved confinement and high beta in neutral-beam-heated divertor discharges of the asdex tokamak. *Phys. Rev. Lett.*, 49:1408–1412, Nov 1982.

[32] P. Bohm, D. Sestak, P. Bilkova, M. Aftanas, V. Weinzettl, M. Hron, R. Panek, L. Baillon, M. R. Dunstan, G. Naylor, and M. J. Walsh. Laser system for high resolution thomson scattering diagnostics on the compass tokamak. *Review of Scientific Instruments*, 81(10):10D511, 2010.

[33] R. Panek, T. Markovic, P. Cahyna, R. Dejarnac, .J Havlicek, J. Horacek, M. Hron, M. Imrisek, P. Junek, M. Komm, D. Šesták, J. Urban, J. Varju, V. Weinzettl, J. Adamek, P. Bilkova, P. Bohm, M. Dimitrova, P. Háček, and the COMPASS team. Conceptual design of the compass upgrade tokamak. 123, 03 2017.